The Astrophysical Journal, 830:157 (17pp), 2016 October 20 doi:10.3847/0004-637X/830/2/157

DETAILED ANALYSIS OF NEAR-IR WATER (H_2O) EMISSION IN COMET C/2014 Q2 (LOVEJOY) WITH THE GIANO/TNG SPECTROGRAPH

S. Faggi[1,2], G. L. Villanueva[3], M. J. Mumma[3], J. R. Brucato[1], G. P. Tozzi[1], E. Oliva[1], F. Massi[1], N. Sanna[1], and A. Tozzi[1]
[1] Osservatorio Astrofisico di Arcetri, Largo Enrico Fermi 5, I-50125 Firenze (IT), Italy; sfaggi@arcetri.astro.it
[2] Universita' Degli Studi Di Firenze, Dipartimento di Fisica e Astronomia, Via G. Sansone 1, I-50019 Sesto Fiorentino (FI), Italy
[3] NASA Goddard Space Flight Centre, 8800 Greenbelt Rd, Greenbelt, MD 20771, USA
Received 2016 February 9; revised 2016 July 18; accepted 2016 July 27; published 2016 October 19

ABSTRACT

We observed the Oort cloud comet C/2014 Q2 (Lovejoy) on 2015 January 31 and February 1 and 2 at a heliocentric distance of 1.3 au and geocentric distance of 0.8 au during its approach to the Sun. Comet Lovejoy was observed with GIANO, the near-infrared high-resolution spectrograph mounted at the Nasmyth-A focus of the TNG (Telescopio Nazionale Galileo) telescope in La Palma, Canary Islands, Spain. We detected strong emissions of radical CN and water, along with many emission features of unidentified origin, across the 1–2.5 μm region. Spectral lines from eight ro-vibrational bands of H_2O were detected, six of them for the first time. We quantified the water production rate [$Q(H_2O)$, $(3.11 \pm 0.14) \times 10^{29}\,s^{-1}$] by comparing the calibrated line fluxes with the Goddard full non-resonance cascade fluorescence model for H_2O. The production rates of ortho-water [$Q(H_2O)^{ORTHO}$, $(2.33 \pm 0.11) \times 10^{29}\,s^{-1}$] and para-water [$Q(H_2O)^{PARA}$, $(0.87 \pm 0.21) \times 1029\ s^{-1}$] provide a measure of the ortho-to-para ratio (2.70 ± 0.76)). The confidence limits are not small enough to provide a critical test of the nuclear spin temperature.

Key words: astrobiology – comets: individual (C/2014 Q2 Lovejoy) – instrumentation: spectrographs – methods: data analysis

1. INTRODUCTION

The search for water in different astrophysical environments (e.g., pre-stellar cores, hot cores, hot corinos, proto-planetary disks, planetesimals, exo-planetary atmospheres, galaxies) along with the study of water across the entire electromagnetic spectrum is one of the most challenging and interesting topics of astronomy. The importance of water is certainly related to life as we know it.

The chemical and physical properties of water were essential to the emergence of life on Earth; living organisms need a medium in which molecules can dissolve and chemical reactions can take place, and water is the universal polar solvent. Favorable water properties—such as high heat capacity, high latent heat, and the lower density in solid state than liquid state—facilitated the formation and persistence of life on Earth. Moreover, the definition of the circumstellar habitable zone is related to the mobility and stability of water; indeed it is defined as the range of distances from a star for which liquid water can persist on a planet's surface. Thus, Earth's location within the Sun's habitable zone derives from its mean surface temperature being intermediate to the high freezing and the much higher boiling points of water (273 K and 373 K, respectively, at 1 bar pressure).

The origin of Earth's ocean water remains uncertain. The proto-Earth formed as a dry planet close to the Sun but within the frost line where only metals and silicates can condense to form rocky planetesimals. The Moon's cratering record suggests that an impulsive event occurred 700 million years after planet formation, the so-called Late Heavy Bombardment, that was likely triggered by migration of the giant planets. That migration destabilized and scattered planetesimals in the outer disk, causing a huge delivery of icy bodies to the inner part of the solar system (Gomes et al. 2005; Jewitt et al. 2008). Many others were delivered to the Kuiper Belt and Oort cloud reservoirs.

Water is the most abundant native (primary) ice in cometary nuclei, so the natural question that scientists consider is: did comets deliver water to Earth? Measurements of spin-isomeric (from ortho and para nuclear spin isomers) and isotopic ratios (from H_2O and HDO) can test the environment in which water formed, since both markers are sensitive to formation temperature (Mumma et al. 1987; Villanueva et al. 2012). From previous investigations of water's hydrogen isotopic ratio (D/H) in various bodies of the solar system, the origin of terrestrial water was attributed for the most part to small bodies like comets and asteroids.

The D/H ratio in several comets from the Oort cloud returned a value about twice that in Earth's oceans, suggesting that comets delivered only ~10% of that water (Morbidelli et al. 2000; Izidoro et al. 2013). The *Herschel Space Telescope* changed that view significantly: the ratio in C/2009 P1 Garradd ($2.06 \pm 0.22 \times 10^{-4}$) was only slightly higher than that in standard mean ocean water (VSMOW, $1.5576 \pm 0.001 \times 10^{-4}$; Bockelée-Morvan et al. 2012). For water in Jupiter Family Comets (JFCs), *Herschel* returned a D/H ratio of $1.61 \pm 0.24 \times 10^{-4}$ in 103P/Hartley 2 (in agreement with VSMOW; Hartogh et al. 2011), and the ratio in 45P/H-M-P (Lis et al. 2008) was less than 2.0×10^{-4} (3-σ), and consistent with the Hartley 2 result. But in 67/P Churyumov–Gerasimenko, the ROSINA investigation on Rosetta returned a much higher value for the D/H ratio in water—$(5.3 \pm 0.7) \times 10^{-4}$, about three times greater than VSMOW (Altwegg et al. 2015). This high value may suggest that such icy bodies did not deliver Earth's water—or perhaps that we need to better understand how our planetary system formed, how this comet nucleus evolved, and whether the measured D/H ratio represents the bulk value in the nucleus of 67P. Values of D/H even smaller than VSMOW are expected for some JFCs owing to radial dispersion in the proto-planetary disk, and Oort cloud comets exhibit a range whose lower

values approach VSMOW (Mumma & Charnley 2011; Bockelée-Morvan et al. 2012).

Detailed knowledge on the composition(s) of cometary nuclei is necessary to understand the formation and evolution of primordial matter across the early solar system. These icy bodies can play a key role in testing the origin of Earth's water, because their composition(s) reflects the distance(s) at which the pre-cometary ices formed.

The infrared wavelength range is a powerful tool for studies of primary volatiles (i.e., native to the nucleus, aka parent molecules). Such primary volatiles are released into the cometary coma where they can be detected through solar-pumped fluorescent emission at infrared (IR) wavelengths. Solar radiation excites IR-active molecules to both fundamental and high-energy vibrational levels (collisions, scattered light and thermal emission from both grains and nucleus excite vibrational modes only inefficiently). Collisional relaxation is slow in the low-density cometary coma, so the pumped molecules quickly emit at IR wavelengths through a complicated pathway of fluorescence cascade.

Using this approach, water in comets was detected directly for the first time in 1985 December, when ro-vibrational lines of the ν_3 band of water were observed in comet Halley using high-dispersion IR spectroscopy from NASA's Kuiper Airborne Observatory (KAO) (Mumma et al. 1986). In 1986 March, water was again detected from the KAO (Larson et al. 1986; Weaver et al. 1986) and the IKS IR spectrometer aboard *Vega 1* detected the ν_1 and ν_3 bands of H_2O near 2.7 μm (Combes et al. 1986, 1988). Further water detections were obtained with the moderate-resolution spectrometer of the *Infrared Space Observatory* in comet C/1995 O1 (Hale–Bopp) (Crovisier et al. 1996).

Ground-based detections of cometary water were enabled by the advent of CSHELL at the NASA IRTF (Infrared Telescope Facility), the first 2D array-based cryogenic IR spectrometer to cover the wavelength region of 1–5.5 μm at high resolving power (RP $= \lambda/d\lambda \sim$ 30,000). Using it, searches for H_2O first emphasized emission lines of the (111–100) vibrational hot-band near 2 μm, and single lines were first detected in C/1991 T2 (Shoemaker–Levy) and 6P/d'Arrest (Mumma et al. 1995). With an improved detector array in 1996, 13 H_2O lines were detected in comet C/1996 B2 (Hyakutake) and water production was quantified (1.7×10^{29} mol s^{-1}, (Mumma et al. 1996); the production rates were later revised slightly as improved fluorescence models were developed (Dello Russo et al. 2002). In the region near 4.7 μm, strong non-resonance fluorescence emissions of water hot bands (100–010) and (001–010) were detected in comet Hyakutake (Mumma et al. 1996) and were later emphasized in C/1995 O1 (Hale–Bopp) (Dello Russo et al. 2000). However, with Hale–Bopp and later comets, attention shifted to H_2O emissions in the 2.9–4.7 μm region, where water and other volatile species could be detected simultaneously. This method became a standard one for measuring water production rates in comets.

Today, the high-resolution IR spectrograph GIANO mounted on the TNG telescope enables detection of the full 0.9–2.5 μm wavelength range in a single exposure, with resolving power ($\lambda/d\lambda$) approaching 50,000. Other high-resolution spectrographs are available nowadays; for example iGRINS at the McDonald Observatory covers a portion of this range (H & K bands only, at $\lambda/d\lambda \sim$ 40,000), while iSHELL at NASA IRTF (0.8–5.5 μm, at $\lambda/d\lambda \sim$ 80,000) will be available for on-sky use in 2016, and similar instruments such as CRIRES+ at the VLT will be commissioned in 2017. GIANO can cover the YJHK IR-bands in a single exposure with very high resolving power, and the results presented here represent the first application of these emerging instruments to a comet.

In this paper, we present spectra of comet C/2014 Q2 Lovejoy collected at TNG across the 50 orders of the GIANO echellogram, from which we quantify the H_2O rotational temperature (T_{rot}), the ortho- and para-production rates and their ratio (the ortho-para ratio (OPR)), and the total water production rate [$Q(H_2O)$]. We detected eight vibrational water bands: (111–100), (021–010) and (011–000) near 2 μm and (201–100), (210–010), (111–010), (200–000), and (101–000) near 1.4 μm. When compared with trace gas abundances, these water measurements can contribute to understanding the volatile composition of comet Lovejoy and its place in the emerging chemical taxonomy of comets.

2. OBSERVATIONS AND CALIBRATION

Terry Lovejoy, using a 0.2 m Schmidt–Cassegrain telescope, discovered this namesake comet on 2014 August 17. Comet C/2014 Q2 Lovejoy (hereafter Lovejoy) is a long-period comet with aphelion near 1165 au ($1/a = 0.0017171$ au^{-1}) and perihelion near 1.29035 au (Nakano Note, NK2831). The Tisserand parameter (0.246, with respect to Jupiter) identifies the comet as being from the Oort cloud, and its present (small) value of aphelion corresponds to the inner Oort cloud. It is not known whether comet Lovejoy is now making its first perihelion passage since emplacement in the Oort cloud. During its approach to the Sun, the comet made a close passage to Earth at 0.46885 au on 2015 January 7, and was still favorably placed during our observations.

2.1. Observations

We conducted astronomical observations of comet Lovejoy with GIANO, the new near-IR high-resolution spectrograph mounted at the Naysmith-A focus of the TNG (Telescopio Nazionale Galileo) in La Palma, Canary Islands, Spain. GIANO provides cross-dispersed echelle spectra at a resolving power of $\lambda/\Delta\lambda \sim$ 50,000 over the 0.95–2.45 μm spectral range, in a single exposure (50 orders). Spectral coverage is complete for wavelengths below 1.72 μm, i.e., from order 45 to order 81. At longer wavelengths (orders 44–32) a few small windows fall outside the detector, making the effective coverage ~75% for the final order (32).

The instrument is fed by two IR-transmitting fibers (85 μm diameter) that each cover 1″ angular diameter on the sky (~727 km at 1 au). The two fibers are spaced at a fixed separation (centre-to-centre) of about 250 μm, i.e., 3″ in the sky plane. GIANO is equipped with a 2048 × 2048 HAWAII-2 PACE detector. Details of the instrument parameters are given in Table 1.

We observed comet Lovejoy near perihelion from 2015 January 31 to 2015 February 2, when the comet was at a heliocentric distance (R_h) of 1.29 au and geocentric distance of about 0.8 au (perihelion was UT January 30.07 at $R_h = 1.29035$ au). The large geocentric Doppler shift (~33 km s^{-1}) shifted cometary emission lines away from their corresponding terrestrial atmospheric absorption lines. In this paper we present results obtained from data collected on February 2.

The presence of two fibers allows GIANO to acquire spectra of point astrophysical objects and sky simultaneously; the sky

Table 1
GIANO's Parameters

Detector	HAWAII-2 PACE 2048 × 2048
Pixel size	18 μm, 0.25 arcsec on sky
Gain	2.2 e-/ADU
Readout Noise	5 e-/pixel
Dark Current	0.05 e-/s/pixel
Saturation level	~18000 ADU/pixel
Spectral Coverage	0.95–2.45 μm
Spectral Sampling	2 pixels at $R \sim 50{,}000$
Spatial Sampling	4 pixels for 1 arcsec fiber

can later be subtracted, thanks to the nodding mode AB. We observed the flux standard star Hip 029216, an O6 star with $M_V = 7.55$, obtaining spectra of both star and sky and we removed sky emissions (mainly lines of OH Meinel bands) from the stellar data by subtracting A and B frames. However, the comet was an extended source and its angular dimension at a geocentric distance of 0.8 au exceeded the fiber spacing (3″) and the coma even overlapped the second fiber. Nodding AB on the comet did not allow us to acquire spectra of the object and the sky separately and simultaneously; indeed the A and B beams sampled different areas of the cometary coma when nodded. We adopted the observational strategy shown in Figure 1. By placing the nucleus in (first) the A and (then) the B beams, we acquired simultaneous spectra of the nucleus and two different portions of the coma, which hereafter we term "nucleus," "coma up" and "coma down" positions.

On February 2, we acquired comet spectra in five nod pairs (AB cycles), in each cycle using 300 s of integration time with the nucleus region centered in fiber A and 300 s with it centered in B; later we acquired sky frames (using the same integration time), shifting the telescope of 800″ in right ascension (R.A.). Calibration lamps (halogen for flat-field and U-Ne for wavelength calibration) and dark frames were also acquired. Observational details are summarized in Table 2.

2.2. Data Reduction and Flux Calibration

A typical GIANO echellogram is shown in Figure 2, Panel A. The echellogram frame grasps 50 orders, from order 32 (at bottom) to order 81 (at top). Each order shows the output of two fibers, so for every order we should expect two arc-shaped tracks.

However, the output of each fiber is split in two by an image-slicer, so each order is actually composed of four arc-shaped tracks, as seen more clearly in the zoom-panels (Figures 2(B), (C), (D)). For clarity, we named "track 1" and "track 2," the two tracks extracted from fiber A and "track 3" and "track 4" the two tracks extracted from fiber B. In total, there are 200 arc-shaped tracks. Each spectral order (group of four tracks) contains a part of the spectrum falling inside a wavelength sub-range. Wavelength ranges for each order are listed in Appendix A and a few examples are shown in Figure 2(A) for clarity (boxes B, C, D). The zoom of box B (Figure 2(B); orders 68, 69, 70 and 71) shows fluorescent emission of radical CN near 1.1 μm. The zooms of box C (Figure 2(C); orders 53, 54, 55 and 56) and box D (Figure 2(D); orders 39, 40, and 41) show fluorescent emission lines of eight combination bands of H_2O in the 1.4 and 2.0 μm wavelength regions, respectively.

The 2D spectra have been processed using *GIANO_tools*, a collection of routines available in any basic installation of IRAF (Image Reduction and Analysis Facility developed by the NOAO), along with some additional ad hoc scripts developed and adapted by GIANO team[4] for reducing GIANO spectra.

The routine *GIANO_tools* performs bad-pixel correction of flat-field, reference lamp, science, and calibration frames. We first form a pair of mean dark frames (300 and 60 s) from the individual dark frames taken at 300 and 60 s (Table 2), and the appropriate mean dark frame is then subtracted from each data frame (comet, star, sky, flat, lamp) to remove dark current levels pixel-by-pixel. *GIANO_tools* then divides each dark-corrected lamp, science, and calibration frame by the normalized flat-field frame. Finally, *GIANO_tools* extracts and wavelength-calibrates the 200 1D spectra from each frame.

The cleaned 1D spectra were processed using custom software developed by Villanueva and Faggi to flux-calibrate the GIANO spectra. We flux-calibrated the 200 1D spectra (extracted from a GIANO echellogram), using an improved version of the advanced GENLN3 terrestrial model (Edwards 1992; Villanueva et al. 2015). The model synthesizes the transmittance and radiance spectra of Earth's atmosphere across the GIANO spectral range (0.9–2.5) μm for the specific observing conditions, allowing us to reproduce and subtract absorption features that are present in the standard star and/or cometary continuum in order to properly calibrate the cometary spectra. The GENLN3 model creates the synthetic spectrum that accounts for telluric lines of H_2O, CO_2, CO, O_3, N_2O, CH_4, O_3, NH_3, and C_2H_6, and convolves the fully resolved synthetic spectra of our atmosphere to the GIANO spectral resolution.

In order to flux-calibrate our spectra we evaluated the expected fluxes [W cm^{-2} μm^{-1} s] of the standard star (Hip 029216) at the top of Earth's atmosphere achieved from the magnitudes of the star in J, H and K center bands; we linearly interpolated the values across all the GIANO spectral range, and we convolved this expected flux with a second-order polynomial function representing the efficiency function. Then, we multiplied the convolved synthetic spectrum of Earth's atmosphere (transmittance model) by the flux of the standard star convolved with the polynomial function and we used it to achieve the best fit of the measured standard star spectrum. The fitting process yields the conversion efficiency (Γ) from stellar flux density (W cm^{-2} μm^{-1}) to counts (ADU/s) per pixel across each spectral order. The cometary spectra were then calibrated using the obtained conversion efficiencies. In Appendix B, we list the mean value of efficiency functions (Γ, in units of [W cm^{-2} μm^{-1}]/ADU s^{-1}) for each track and for each order. After the flux-calibration we fitted the cometary spectra with the terrestrial synthetic atmosphere model in order to properly remove the absorption features affecting continuum and achieve in this way molecular residual spectra.

Next, the calibrated molecular residual 1D spectra (and simultaneously the calibrated cometary spectra (before the continuum subtraction) and the continuum modeled spectra) were combined according to the cometary area they sampled (i.e., the nucleus area was sampled alternatively by fiber A (with tracks 1 and 2) and by fiber B (with tracks 3 and 4). Thus, we combine spectra from tracks 1 and 2 for fiber A with those

[4] http://www.tng.iac.es/instruments/giano/

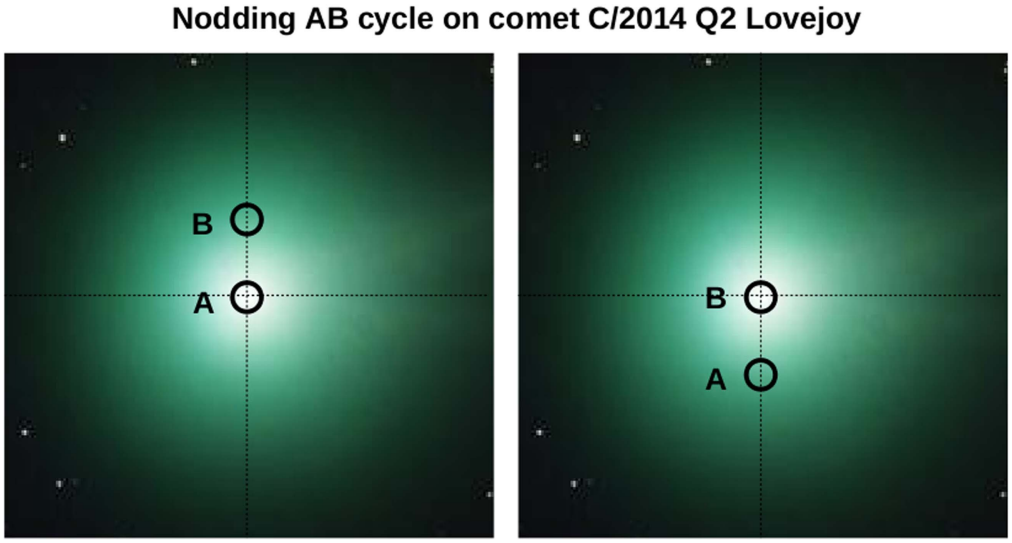

Figure 1. Two panels show the observational setup and nod strategy adopted when observing comet Lovejoy. The 1″ diameter fibers, called A and B, are spaced by 3″ in the sky plane. During the telescope pointing, one fiber is centered on the photometric nucleus of the comet and the second samples the coma 3″ off the nucleus. The nodding permits sampling of three different regions: the upper part of the coma (B fiber on left panel), the nucleus (A fiber on left panel and B fiber on right panel) and the lower part of the coma (A fiber on right panel). The appropriate combination of these samples allowed us to achieve three different positional samplings of the comet.

from tracks 3 and 4 for fiber B to produce a residual for the nucleus sampled area. Similar processes were performed to obtain spectra for coma up and coma down regions.).

An example of flux-calibrated cometary spectra and the process of continuum subtraction are shown in Figure 3, top plot. The cometary spectrum (black) and modeled continuum (red; as affected by terrestrial atmospheric transmittance) are shown. An example of cometary molecular residual (after continuum subtraction), of the modeled spectrum for fluorescent water emission, necessary to identify and characterize the detected lines, and of the observed sky spectrum, useful to show the sky emission lines, are shown in the bottom part of Figure 3. In Figure 4, we also show residual spectra of the three sampled cometary area for order 40 of the GIANO echellogram : the *center* (i.e., *nucleus-centered*) spectra, the *coma up* spectra, and the *coma down* spectra; we proceeded the water fluorescence analysis on these spectra.

A detailed analysis of noise, reported in Appendix C, showed that the measured noise is in agreement with the expected noise.

3. WATER FLUORESCENCE ANALYSIS

We can derive column densities, rotational temperatures, and production rates for primary volatiles from their observed ro-vibrational lines, if the main excitation and emission processes are understood.

In general the excitation process is led by two principal mechanisms.

1. Radiative excitation: solar radiation can directly excite fundamental vibrational states of IR-active gases in comets (Mumma 1982; Yamamoto 1982; Crovisier & Encrenaz 1983; Weaver & Mumma 1984). This was first confirmed by the detection of ν_3 fundamental band emissions in comet 1P/Halley, but the serendipitous discovery of ν_3 hot-band emission (011–010) demonstrated that combination-band pumping followed by cascade is also important (Mumma et al. 1986; Weaver et al. 1986).[5]
2. Collisional excitation: in general, collisions with gaseous molecules[6] and/or electrons control the rotational excitation of molecules in the inner coma. Within ∼2 au of the Sun, water ice is fully activated and H_2O becomes the most abundant primary gas in the cometary coma. However, at distances greater than ∼2 au water ice is increasingly stable and by about ∼4 au more volatile ices dominate gaseous release from the nucleus, with first CO_2 and/or then CO replacing the role of H_2O.

Neutral–neutral collisions can affect the excitation of coma gases, in several ways. (i) Collisions can de-excite vibrational levels at nucleocentric distance (r) $\leqslant$ 20 km. If frequent enough, collisions can kinetically quench vibrationally excited molecules, thereby reducing the radiative emission of vibrational bands near the nucleus surface—but this process is generally unimportant at greater nucleocentric distances (see Crovisier & Encrenaz 1983; Weaver & Mumma 1984). (ii) Collisions can excite vibrational levels. This process is generally negligible because of both the relatively high energy of vibrational levels and the low kinetic temperature of the inner coma. (iii) Collisions can thermalize rotational levels in the innermost coma. This process is efficient, but for polar species it must compete with radiative relaxation and other effects and so is effective only at sufficiently high collision rates. Owing to their high cross sections with water, collisions with electrons are far more effective and can thermalize water

[5] Apart from direct solar radiation pumping, the molecular vibrational bands can be radiatively excited by radiation from the nucleus and dust grains, produced by both scattering of solar radiation and by their own emission in the thermal IR. However, these processes are negligible in the inner coma, except excitation owing to dust thermal emission that can be important in the inner comae of active comets at thermal IR wavelengths (Crovisier & Encrenaz 1983; Weaver & Mumma 1984).

[6] Water is inactive at large heliocentric distances, permitting CO and other still volatile gases to dominate the inner coma and control collisional excitation of trace species.

Table 2
Observing Parameters

Object	Date/Time (UT hr:mn)	Int. Time (s)	N exp.	R_H (au)	Δ (au)	Δ (km s^{-1})
C/2014 Q2 Lovejoy	2015 Jan 31 21:00	300	3 nodding AB	1.29	0.77	32.78
Hip029216	〃	…	…	…	…	…
Flat	〃	60	5	…	…	…
Sky	〃	300	7 stare	…	…	…
U-Ne Lamp	〃	300	1	…	…	…
Dark	〃	300–60	10–10	…	…	…
C/2014 Q2 Lovejoy	2015 Feb 01 21:00	300	5 nodding AB	1.29	0.79	33.07
Hip029216	〃	300	3 nodding AB	…	…	…
Flat	〃	60	5	…	…	…
Sky	〃	300	7 stare	…	…	…
U-Ne Lamp	〃	300	1	…	…	…
Dark	〃	300–60	10–10	…	…	…
C/2014 Q2 Lovejoy	2015 Feb 02 21:00	300	5 nodding AB	1.29	0.81	33.31
Hip029216	〃	300	3 nodding AB	…	…	…
Flat	〃	60	10	…	…	…
Sky	〃	300	11 stare	…	…	…
U-Ne Lamp	〃	300	1	…	…	…
Dark	〃	300–60	10–10	…	…	…

rotational levels even in the medium coma, for $r \leqslant 10^4$ km (Xie & Mumma 1992).

The coma is an environment characterized by low temperatures, from 50 to 200 K, and low molecular densities (from values of about 10^{12} cm^{-3} near to the nucleus surface of a moderately active comet to interplanetary values of about 1 cm^{-3} in the outer coma), so in such conditions, it is plausible to assume that neutral–neutral collisions cannot excite the vibrational levels of molecules for which $E_{vib} \gg kT$. However, they can thermalize the rotational population of ground vibrational state, $(\nu_1\nu_2\nu_3) = (000)$, at the kinetic temperature of the gas, so it is possible to assume local thermodynamic equilibrium (LTE) in the ground vibrational state (Xie & Mumma 1992).

In the medium cometary coma, the rotational population of ground vibrational level of H_2O is maintained at LTE by electron collisions and the main vibrational excitation process is radiative excitation by direct solar radiation. Once excited, water molecules can emit photons at IR wavelengths through a rapid cascade called fluorescent emission, either to the ground vibrational state (so-called *resonance fluorescence*) or to various intermediate energy levels (*non-resonance fluorescence*) with relative efficiencies given by their branching ratios.[7] Fluorescence emission is the main phenomenon observed for primary volatiles in cometary coma at IR wavelengths (OH prompt emission is an important direct proxy for water emission). (At radio and sub-mm wavelengths, the principal emission mechanism is thermal emission from excited rotational levels in the ground vibrational state.) High-resolution spectrometers such as GIANO can detect these fluorescent emission lines. Using such data and powerful theoretical models, it is possible to characterize the chemical composition of cometary comae with high precision.

We detected 52 water lines in the 2 and 1.4 μm regions of the GIANO echellogram (Figure 4). These lines represent eight vibrational water bands. In the 2 μm region (orders 39–40–41), we detected two bands in non-resonance fluorescence (111–100) and 021–010) and one band (011–000) in resonance fluorescence, whereas in the 1.4 μm region (orders 53–54–55–56) we detected three non-resonant bands (201–100, 111–010, and 210–010), and two resonant bands (200–000 and 101–000). The band ID for each line is shown in Figure 5.

We used an advanced quantum mechanical fluorescence model for vibrational bands of H_2O to analyze the water emission lines observed in comet Lovejoy. The model evaluates fluorescence efficiencies (g-factors, s^{-1}) using realistic solar spectral fluxes shifted to a comet's heliocentric velocity at the time of observation[8] (Villanueva et al. 2012). Results are given in Table 3.

A careful and detailed study of every detected line led us to discard lines affected by the following issues:

1. Contamination by residual sky emission: sky lines can be present in our cometary spectra for two systematic reasons, even if the sky emission does not vary with time. First, we took data with the comet centered first in the A-fiber and then in the B-fiber. Taking data in this ABAB mode will generally ensure a mismatch in the sky emission since the air masses of sequential (A, B) frame pairs differ by the same amount. Although both fibers are sampled simultaneously, we chose not to subtract the on- and off-nucleus spectra, because the nucleus-centered coma emission would then be reduced by the off-nucleus coma flux. Accordingly, sky frames were acquired after comet observations, with the telescope shifted by 800 arcsec in R.A. from the comet position. This approach prevents exact cancellation of sky emission, instead leaving a positive or negative residual owing to the

[7] In the outer coma, collisions cannot maintain the rotational states in LTE. Instead, their populations are set by the balance between solar pumping and subsequent spontaneous decay (known as fluorescence equilibrium).

[8] Fluorescence efficiencies (g-factors) can depend on the Doppler shift in cometary gas relative to the Sun, especially in spectral regions with crowded Fraunhofer lines (e.g., the CN violet system) or where the solar spectrum contains spectral lines of the same species as sought in the comet (e.g., CO). This effect takes two forms: the "Swings effect" stems from the frequency shift produced by heliocentric velocity of the comet's motion (Swings 1941), while the "Greenstein effect" stems from the shift in frequency due to the motion of molecules in the cometary coma (Greenstein 1958). The latter effect is usually considered negligible.

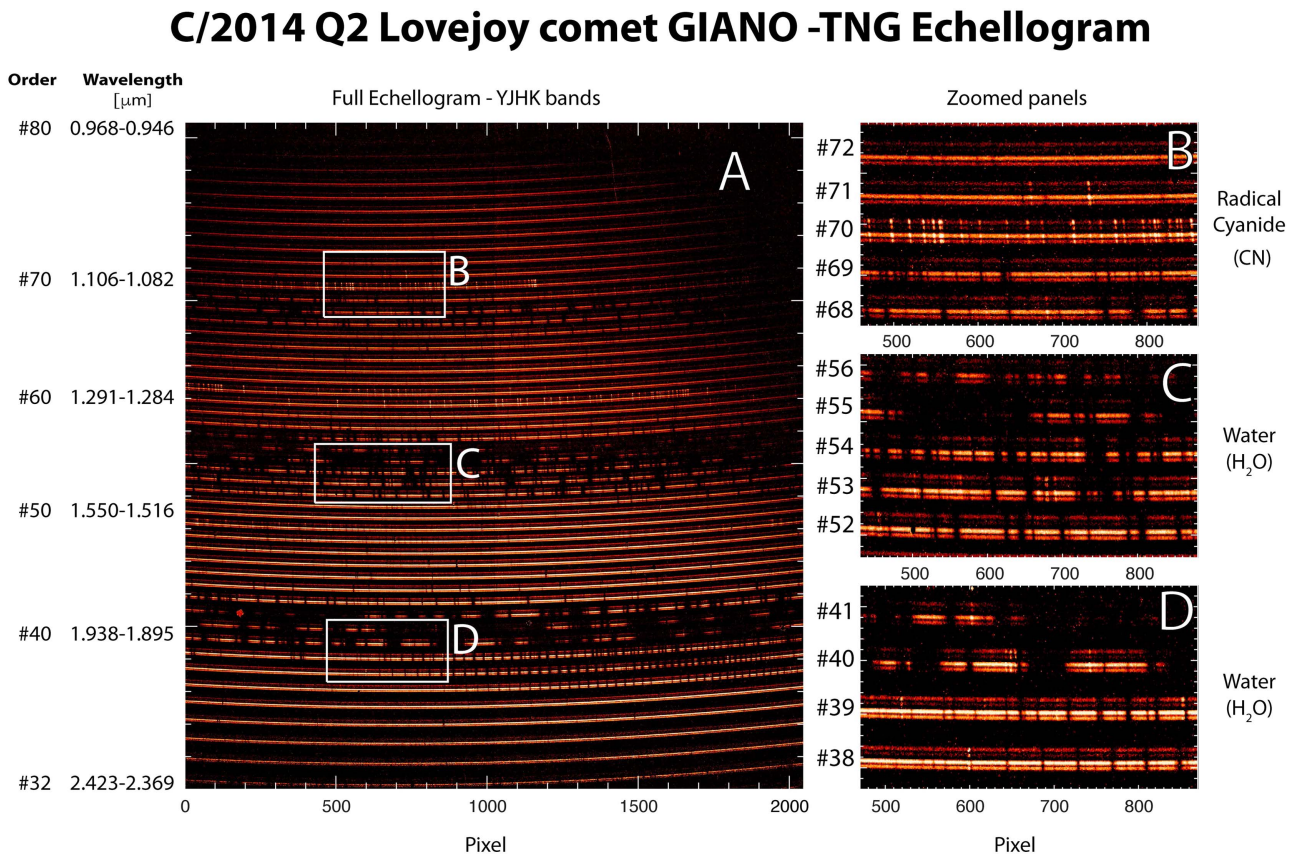

Figure 2. Panel A: GIANO echellogram of comet Lovejoy acquired on UT 2015 February 2. The panel shows the full echellogram covering 50 orders. Pixel column number (*x*-axis) and order number and wavelength range (*y*-axis) are labeled. The order number increases from the bottom (#32) to the top (#80). Wavelength decreases from left to right within each order, and decreases from bottom to top across the echellogram. Each order contains a group of four arc-shaped tracks. The upper two tracks (3, 4) of each group correspond to image slices of fiber B and the lower two tracks (1, 2) to fiber A (slices); in this frame the photometric nucleus of comet was centered on fiber A, where strong cometary continuum is seen in all orders. Absorption features of terrestrial atmospheric gases appear throughout the echellogram (e.g., at the top and bottom of H band), along with many sky emission lines of OH (Meinel bands) that fill the fibers uniformly so are equally bright in tracks 1, 2, 3, and 4. We outline regions in which we detected cometary water and radical CN. Cometary H_2O lines are brighter near the nucleus (tracks 1 and 2) but also appear in the off-nucleus position (3 and 4). The lines of radical CN (a product species) are equally bright in tracks 1, 2, 3, and 4. Zoomed panels B-D: pixel column and order numbers are shown on the *x*- and *y*-axis, respectively. Panel B shows zoomed box B from panel A (near 1.1 μm) in which radical CN and probably water are detected. Panels C and D show the water vibrational bands near 1.4 and 2 μm detected in boxes C and D (panel A).

difference in air mass during integration on the sky and on the comet.[9] Moreover, the principal sky emissions (OH Meinel bands) vary with time, introducing a second factor that limits sky cancellation of such emission even if taken at the same air mass but at different times. Most recent analysis of OH Meinel bands system, detected with GIANO, is reported in (Oliva et al. 2013, 2015).

2. Baseline problems: baseline issues can be introduced by diverse effects such as imperfect sky subtraction or imperfect modeling of the cometary continuum convolved with the synthesized terrestrial atmospheric transmittance.
3. Misfit in shape: the presence of embedded emission lines from other molecules (or even from H_2O) could cause the measured shape of a cometary line to differ from that predicted by the fluorescence model.
4. Misfit in intensity: the non-perfect evaluation of some fluorescence model parameters could contribute to a misfit between predicted and measured intensity.

We included only lines that were labeled as "*OK*," "*Noisy*," or "*Trn*" (Figure 5) when evaluating column densities, fluxes at top of the atmosphere and production rates for ortho-water and para-water. The "*Noisy*" label means that these lines are in a noisy continuum and the "*Trn*" label means that the transmittance evaluated for that line was $<10\%$. A quantitative description for each of the 52 detected lines is given in Figure 5 and reported in Table 3. The label "*Base*" indicates a line with baseline problems, "*Shape*" a line with misfit in shape, and "*Int*" is used for a line with misfit in intensity.

3.1. Rotational Temperatures

We observed comet Lovejoy with the two 1″ angular diameter fibers (about 700 km) placed at a fixed center to center distance of 3″ (about 2100 km at the comet on February 2). This means that we observed three different regions in the medium coma, each sampled by a circular beam of 700 km diameter: one region targeted the photometric center and two

[9] OH airglow emission lines dominate sky spectra in GIANO's spectral range. We are able to identify them thanks to precise line lists, but a good quantum mechanical model for OH chemiluminescent emission in our atmosphere is not available. Sky emission lines are also variable with time and variable with altitude so the only way to identify and remove them from a cometary spectrum is by making direct sky observations.

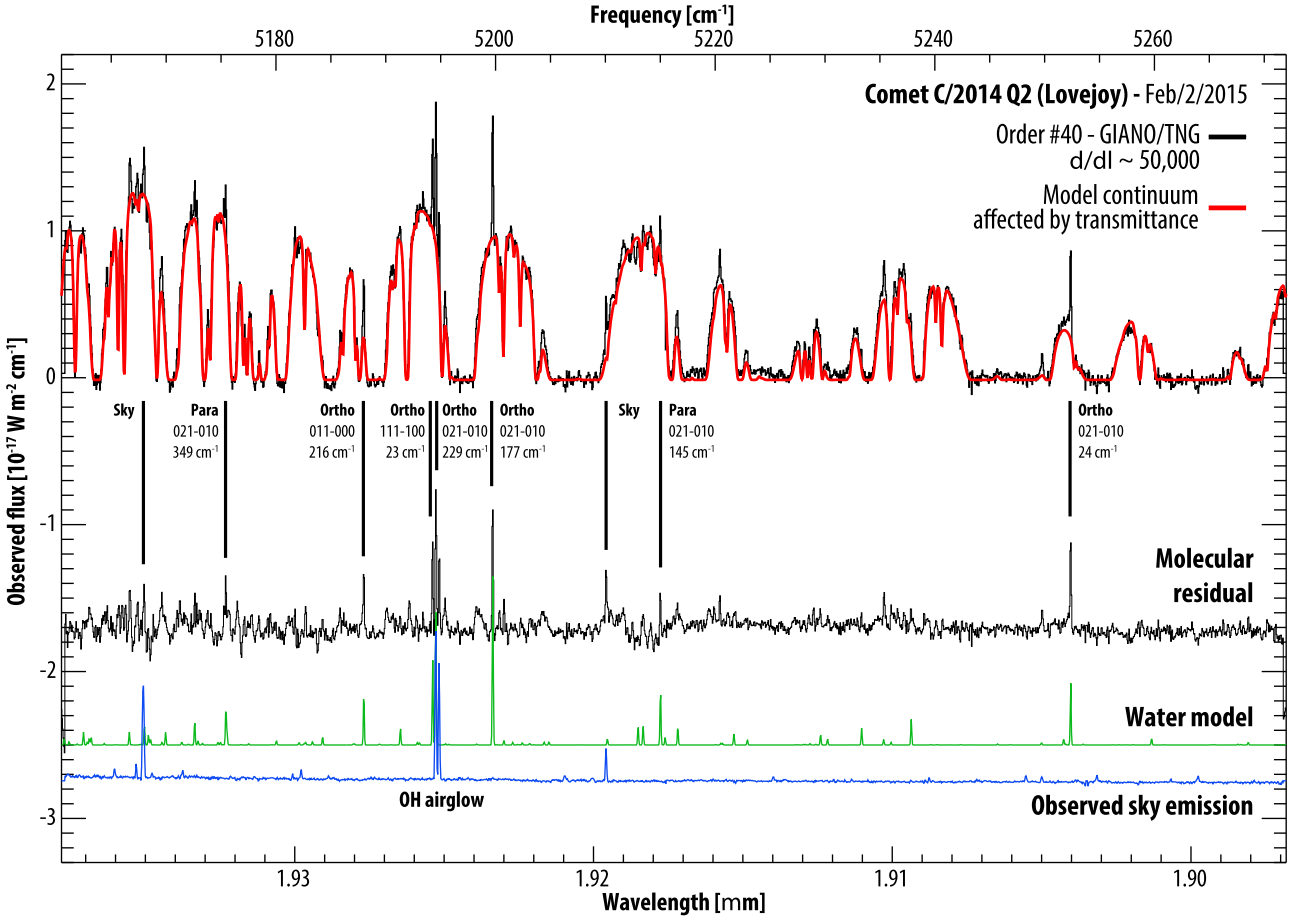

Figure 3. Reduction and identification process by showing cometary spectra from order 40 of a GIANO echellogram. The observed fluxes [10^{-17} Wm^{-2}/cm^{-1}] are shown vs. wavelength (frequency). The scale of the *x*-axis is shown in frequency [cm^{-1}] at top, and in wavelength [μm] at bottom. The topmost trace compares the calibrated cometary spectrum (black) with the (normalized and superimposed) model of continuum affected by terrestrial transmittance (red), while their difference (the residual spectrum) is shown in the next lower trace. The lowest two traces are a synthetic model of cometary water fluorescence (green; Villanueva et al. 2012)) and the observed sky emission (blue). The latter three spectra are shown shifted downward along the *y*-axis relative to the measured cometary spectrum, for clarity. We identified cometary emission lines by comparing the residual cometary spectrum with the spectra of modeled water fluorescence and measured sky emission (see labels above the cometary residual spectrum). Each label identifies the responsible nuclear spin isomer (ortho, para), quantum numbers for the vibrational band, and the rotational energy of the ground state.

regions sampled the coma at ± 2100 km from the photocenter (see Figure 1 for observation set-up).

The rotational temperature ($T_{\rm rot}$) of a molecule is the temperature that defines the population distribution of rotational levels in the ground vibrational state. In the medium coma (50 km $\leqslant r \leqslant 10^4$ km), electron collisions maintain the ground ro-vibrational states at LTE. The population distribution P_i of rotational levels is described by the following equation, according to the Boltzmann statistic:

$$P_i = \frac{\omega_i e^{-Ei/k_B T_{\rm rot}}}{Z(T_{\rm rot})} \tag{3.1}$$

where ω_i is the statistical weight of level i[10], E_i is the energy of the level i, and $Z(T_{\rm rot})$ is the rotational partition function.[11] We used two different methods to evaluate $T_{\rm rot}$: *the slope analysis* and the *correlation analysis* (Figure 6).

The *slope analysis* method extrapolates $T_{\rm rot}$ for the rotation population in the ground vibrational state considering the relation between $F_{\rm obs}/F_{\rm pred}$, the observed-to-redicted flux ratio, and $\langle E_{\rm pump}^{(000)} \rangle$ the mean value of rotational state energies in the ground vibrational state. The predicted fluxes (i.e., the modeled g-factors) depend on $T_{\rm rot}$. The line flux (W m^{-2}) of optically thin ro-vibrational lines is described by the following formula:

$$F_{\rm ul} = \frac{\Omega}{4\pi} h \nu_{\rm ul} g_{\rm ul} \langle N \rangle \tag{3.2}$$

where Ω is the solid angle corresponding to the field of view, $\nu_{\rm ul}$ is the frequency (cm^{-1}), $g_{\rm ul}$ is the g-factor, i.e., the cometary fluorescence emission rate (photon s^{-1}) and $\langle N \rangle$ is the column density (m^{-2}). The g-factors, are given by:

$$g_{\rm ul} = A_{\rm ul} \frac{\sum_{j,\nu=0} n_j g_{ju}}{\sum_j \sum_\nu A_{\rm ul}} \tag{3.3}$$

where $A_{\rm ul}$ is the (Einstein) spontaneous emission coefficient from u-level to l-level, n_j is the fractional population of the jth level, and g_{ju} are the excitation rates due to solar pumping

[10] Each energy level can be composed of a number of degenerate (equal-energy) quantum states; this number is statistical weight ω_j of level j.
[11] Where: $Z(T_{\rm rot}) = \sum_i \omega_i e^{-Ei/k_B T_{\rm rot}}$.

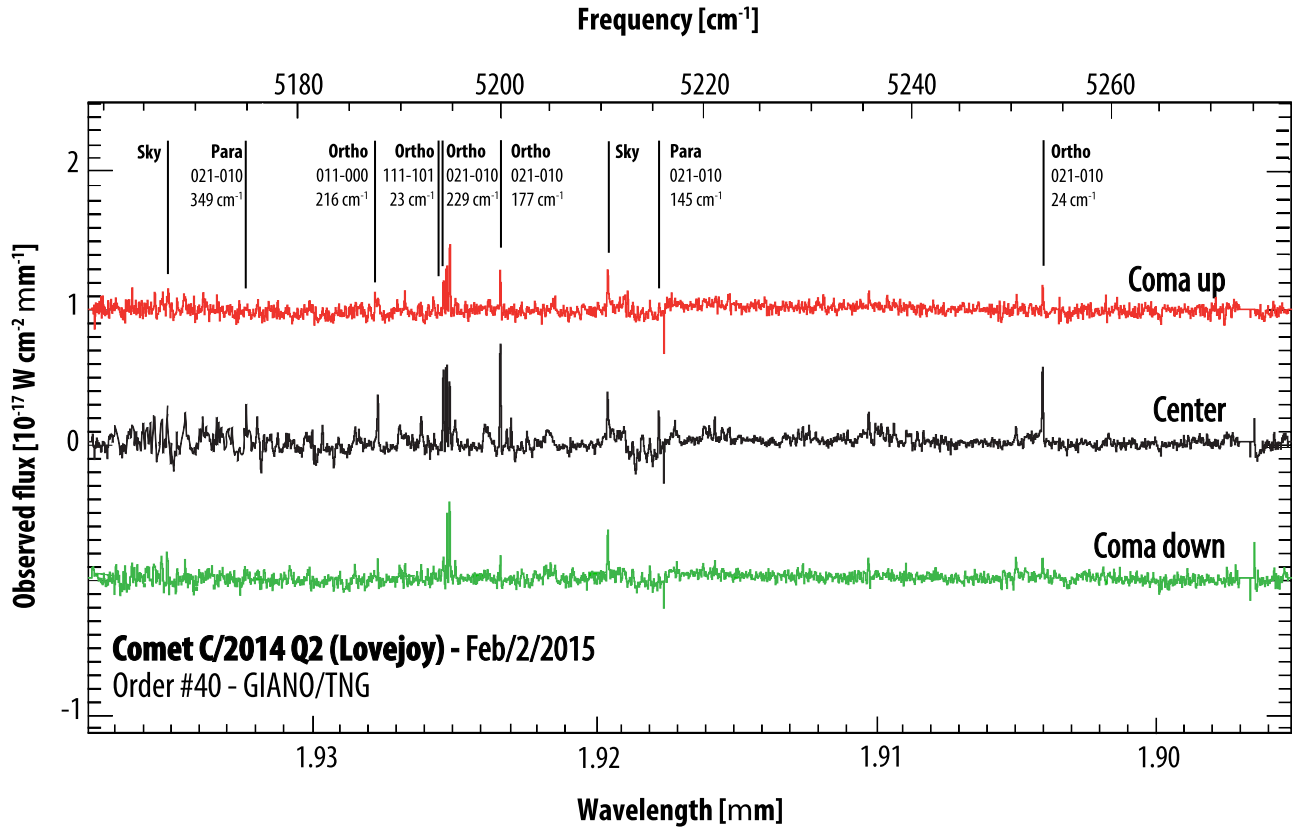

Figure 4. Residuals of cometary spectra from order 40 of the GIANO echellogram are shown. The scale of the x-axis is shown in frequency [cm^{-1}] at top, and in wavelength [μm] at bottom. The three traces are the molecular residuals for the center (black), upper part (red) and lower part of the coma (green). The zero level applies to the coma *center* spectrum, while the *coma up* and *coma down* residuals are shown shifted by $+1$ and -1 unit along the y-axis relative to the *center* residual spectrum, for clarity. Cometary emission lines are identified by comparing residual spectra with spectra of the modeled water fluorescence and of the measured sky emission (see Figure 3). The cometary lines are strongest in the center spectrum, as expected for a primary volatile released from the nucleus.

($g_{\rm pump} = g_{ju}$), defined by the following equation:

$$g_{\rm pump} = \frac{J_\nu B_{\rm lu} \omega_1 e^{-hcE_{\rm low}/kT_{\rm rot}}}{Z(T_{\rm rot})} \quad (3.4)$$

where J_ν is the realistic solar flux received by the comet at frequency ν, $B_{\rm lu}$ is the Einstein coefficient for absorption, ω_1 is the degeneracy of the lower state and $E_{\rm low}$ is the energy of the lower state (Villanueva et al. 2011b).

The line fluxes are related to the populations of rotational levels in the upper vibrational state $E_{\rm up}$ and reflect the temperature dependent distribution of the ground state (000). In general, a single rotational upper state is pumped from several different rotational levels in the ground vibrational state ${E_{\rm pump}}^{(000)}$. The average energy of these lower rotational levels (weighted by their relative contributions to the upper state population) approximates the "mean" energy of the ground state from which they populate the upper state when pumped. At the correct rotational temperature, the ratio between the measured flux and g-factor of the line should be independent of $\langle {E_{\rm pump}}^{(000)} \rangle$. The retrieved rotational temperature is most accurate when a wide range of rotational energy states is sampled.

The quantity described by Flux [Wm^{-2}]/g-factor [W mol^{-1}] is proportional to the column density (see Equation (3.2)). Since the production rate of a molecule is proportional to the column density, a linear fit of Q [s^{-1}] versus $\langle {E_{\rm pump}}^{(000)} \rangle$ should produce a diagram with slope zero within the errors on Q.[12] This diagram is shown in Figure 6, left panel.

The evaluation of an accurate rotational temperature is essential to achieve reliable production rates and, in the slope analysis, this is obtained by comparing all the observed line fluxes (corrected to top of Earth's atmosphere) with respect to the modeled line fluxes, varying the assumed value for $T_{\rm rot}$ until an agreement is found within the errors, across all the observed lines. From the slope analysis the retrieved rotational temperature is about $T_{\rm rot} = (90 \pm 20)$ K.

The *correlation analysis* is based on the comparison between the water model and the observed spectrum.[13] The OPR = 3 is assumed, so the unique free parameter is the rotational temperature $T_{\rm rot}$. The purpose of this method is the evaluation of the correlation coefficient between the observed and the synthetic spectrum, thus identifying the (most probable) temperature that produces the best correlation.

The temperature–correlogram plot (correlogram factor versus $T_{\rm rot}$) is shown in Figure 6 (right panel). The sharper the correlation curve, the better $T_{\rm rot}$ can be constrained by

[12] A value of $T_{\rm rot}$ lower than its optimal value will produce a positive slope. This means that for lines with relatively low rotational energy, the modeled g-factors are overestimated, while for high values of rotational energy they are underestimated.

[13] The retrieval code synthesizes a modeled water spectrum for each value of $T_{\rm rot}$ using the g-factors. After convolution with the resolving power of the instrument, this synthetic spectrum is compared with the observed spectrum.

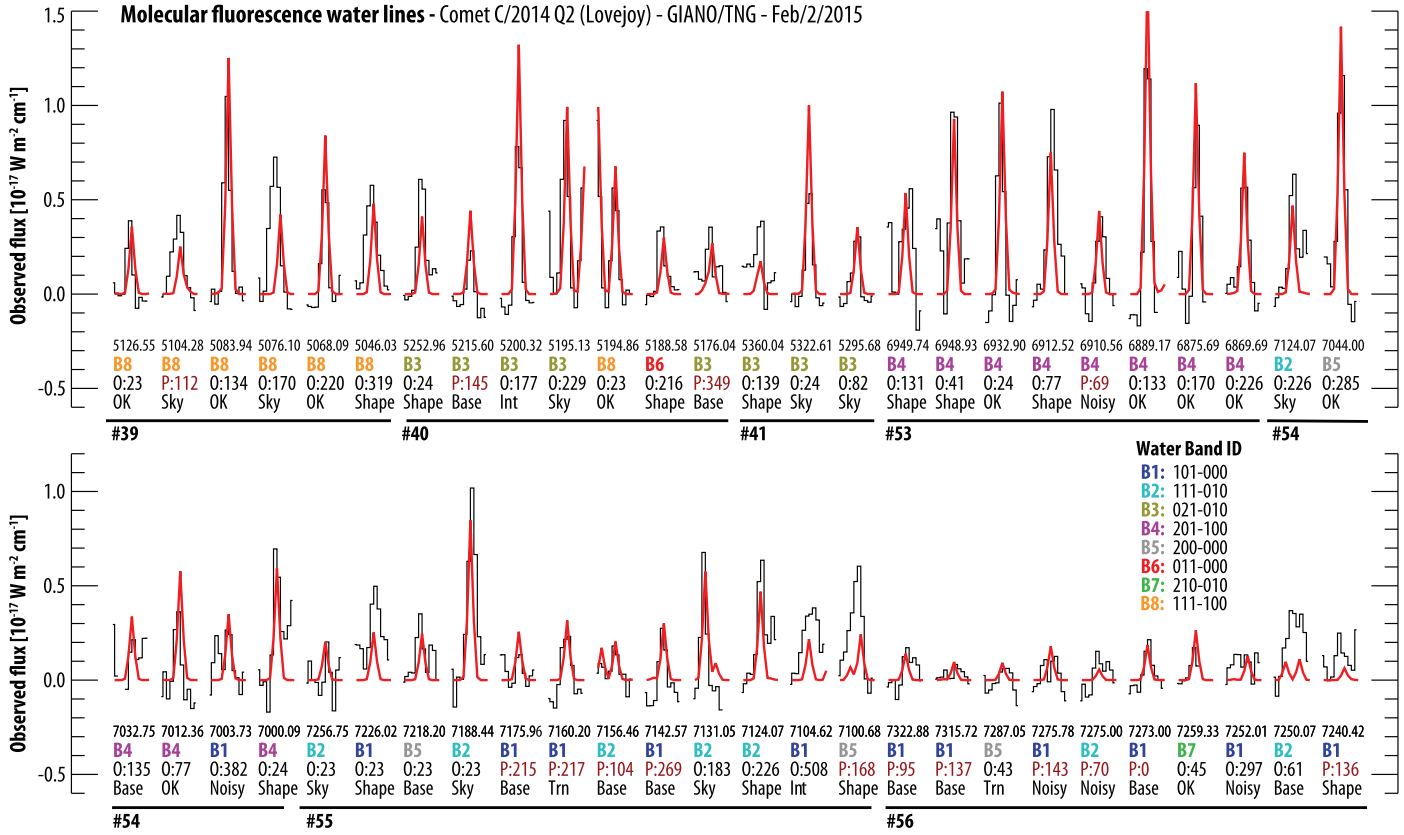

Figure 5. 52 detected lines of water emission in the 1.4 and 2.0 μm regions span seven orders of the GIANO echellogram. The observed positions and intensities of individual lines (black) are compared with predictions of the water fluorescence model (red). On the *y*-axis the observed line flux [10^{-17} Wm^{-2} cm^{-1}] is shown. On the *x*-axis the order ranges (horizontal bars, bold) are reported together with a detailed description of each line. Under each line we show the rest wavenumber [cm^{-1}], the vibrational band ID (B1-B8, see legend at right, lower panel), the nuclear spin isomer (O for ortho, P for para) and the lower energy level [cm^{-1}] (e.g., O:135), and a "quality" label. The labels are: *OK* for a well fitted line, *Noisy* for a line with a noisy continuum, *Trn* for a line with <10% transmittance, *Base* for a line with baseline problems, *Shape* for a line with misfit in shape, and *Int* for a line with misfit in intensity.

the correlation analysis. From the correlation analysis the retrieved rotational temperature is about $T_{\rm rot} = (71 \pm 20)$ K. The evaluation of $T_{\rm rot}$ from the slope and the correlation analyses can also be compared visually (right panel, Figure 6).

3.2. Water Production Rate

We used the slope-zero rotational temperature obtained from the slope analysis (90 K $\pm$ 20 K) to evaluate the total production rate of water in comet Lovejoy.

We assume the Haser model in which water molecules sublimate at the nucleus surface at a constant rate and expand into the coma with spherical symmetry and with uniform velocity. The production rate obtained from a single measured line (Q_i [s^{-1}]) is evaluated as follows:

$$Q_i = \frac{4\pi\Delta^2 F_i^{\rm TOA}}{g_i \tau\,(hc\nu) f\,(x)} \qquad (3.5)$$

where $\Delta[m]$ is the geocentric distance, $F_{\rm i}^{\rm TOA}$ [W m^{-2}] is the flux of the *i*th line, at top of the terrestrial atmosphere (corrected for the terrestrial transmittance at the Doppler-shifted line frequency), g_i [photons s^{-1} mol^{-1}] is the g-factor related to the *i*th line at temperature $T_{\rm rot}$, τ[s] is the molecular lifetime, (hcν) is the energy (in Joules [J]) of a photon with wave number ν(cm^{-1}), and $f(x)$ represents the fraction of total molecules contained in the beam for a symmetric outflow, where x is the scaled, projected displacements of the edges of the aperture from the cometary nucleus.

In Table 3 a detailed description of all the lines is reported. The column labeled as $Q(H_2O)$ lists the total water production rate obtained from each observed line, assuming that the nuclear spin species are in statistical equilibrium (OPR = 3.0).

The total water production rate for 1.4 and 2 μm regions (assuming ortho-to-para ratio equal to 3:1) is $Q(H_2O) = (3.11 \pm 0.14) \times 10^{29}$ s^{-1}. The production rates derived for ortho-water and para-water separately are $Q(H_2O)^{\rm ORTHO} = (2.33 \pm 0.11) \times 10^{29}$ s^{-1} and $Q(H_2O)^{\rm PARA} = (0.87 \pm 0.21) \times 10^{29}$ s^{-1}. These values are the weighted mean of Q obtained from individual line measurements and the uncertainties were determined by comparing the standard deviation from the mean of production rates with the error due to photon noise, and taking the higher value.

The Q[s^{-1}] values, derived from each individual observed line and those taken from different ro-vibrational lines of different bands, showed a general agreement. This reinforces the self-consistency of the data processing algorithms and the fluorescence models used in this investigation.

3.3. Ortho–Para Ratio

In general a molecule that contains identical atoms in spatially symmetric locations shows isomeric symmetries

Table 3
Parameters for Spectral Lines of H_2O Detected in C/2014 Q2 (Lovejoy)

k (cm^{-1})	Band ID ν_{up}–ν_{low}	Line ID J, k_a, k_c	Ortho/ Para	Erot (cm^{-1})	g-factor (10^{-8} s^{-1})	Trans. (%)	Flux TOA (10^{-18} W m^{-2})	Q_{H_2O} (10^{29} s^{-1})
5126.55	111–100	000–101	O	23	1.18	32	1.21 ± 0.31	3.39 ± 0.87
5104.28	111–100	101–202	P	112	0.98	30	2.75 ± 0.38	Sky
5083.94	111–100	202–303	O	134	1.72	75	1.49 ± 0.14	3.00 ± 0.28
5076.10	111–100	211–312	O	170	0.57	77	1.55 ± 0.14	Sky
5068.09	111–100	313–414	O	220	0.90	96	6.19 ± 0.90	2.58 ± 0.38
5046.03	111–100	404–505	O	319	0.50	98	1.11 ± 0.12	Shape
5252.96	021–010	000–101	O	24	2.55	17	5.47 ± 0.34	Shape
5215.60	021–010	212–313	P	145	0.93	49	3.14 ± 0.11	Base
5200.32	021–010	211–312	O	177	2.36	58	1.60 ± 0.99	Int
5195.13	021–010	313–414	O	129	1.85	56	2.95 ± 0.10	Sky
5194.86	111–100	202–101	O	23	1.31	62	1.11 ± 0.91	3.34 ± 0.27
5188.58	011–000	202–321	O	216	1.80	17	2.98 ± 0.32	Shape
5176.04	021–010	312–413	P	349	0.59	55	8.89 ± 0.10	Base
5360.04	021–010	404–303	O	139	0.99	21	3.10 ± 0.22	Shape
5322.61	021–010	202–101	O	24	2.51	41	1.70 ± 0.11	Sky
5295.68	021–010	211–212	O	82	0.75	49	7.67 ± 0.91	Sky
6949.74	201–100	220–221	O	131	0.71	78	2.07 ± 0.36	Shape
6948.93	201–100	111–110	O	41	1.28	75	2.68 ± 0.38	Shape
6932.90	201–100	000–101	O	24	1.37	81	1.75 ± 0.35	3.11 ± 0.62
6912.52	201–100	111–212	O	77	1.20	64	3.61 ± 0.44	Shape
6910.56	201–100	101–202	P	69	0.67	68	8.01 ± 0.42	2.94 ± 0.16
6889.17	201–100	202–303	O	133	2.04	88	2.28 ± 0.31	2.87 ± 0.40
6875.69	201–100	211–312	O	170	1.26	91	1.38 ± 0.30	2.88 ± 0.65
6869.69	201–100	313–414	O	226	0.88	88	1.38 ± 0.31	4.39 ± 0.99
7124.07	111–010	313–414	O	226	1.18	42	3.02 ± 0.35	Sky
7044.00	200–000	221–330	O	285	3.35	44	5.07 ± 0.63	3.80 ± 0.47
7032.75	201–100	404–303	O	135	0.42	84	6.32 ± 0.33	Base
7012.36	201–100	313–212	O	77	0.68	87	4.50 ± 0.31	1.80 ± 1.27
7003.73	101–000	313–432	O	382	0.57	62	1.10 ± 0.44	3.10 ± 1.60
7000.09	201–100	202–101	O	24	1.04	58	1.93 ± 0.47	Shape
7256.75	111–010	202–101	O	23	1.52	14	2.11 ± 0.78	Sky
7226.02	101–000	000–101	O	23	37.4	1	1.95 ± 0.25	Shape
7218.20	200–000	110–101	O	23	2.69	9	8.96 ± 0.18	Base
7188.44	111–010	000–101	O	23	1.60	54	3.81 ± 0.31	Sky
7175.96	101–000	303–322	P	215	0.66	41	4.40 ± 0.42	Base
7160.20	101–000	303–404	P	217	12.4	3	1.17 ± 0.65	2.50 ± 1.40
7156.46	111–010	110–211	P	104	0.49	44	8.04 ± 0.38	Base
7142.57	101–000	312–413	P	269	8.11	4	4.58 ± 0.42	Base
7131.05	111–010	211–312	O	183	1.01	47	3.53 ± 0.28	Sky
7124.07	111–010	313–414	O	226	1.18	42	3.02 ± 0.35	Shape
7104.62	101–000	431–532	O	508	0.98	23	5.01 ± 0.63	Int
7100.68	200–000	111–220	P	168	1.17	28	6.90 ± 0.53	Shape
7322.88	101–000	312–211	P	95	4.31	3	5.29 ± 0.39	Base
7315.72	101–000	321–220	P	137	2.27	5	3.87 ± 0.29	Base
7287.05	200–000	221–110	O	43	2.92	3	4.00 ± 0.42	3.33 ± 3.50
7275.78	101–000	312–313	P	143	1.19	15	2.06 ± 0.86	4.67 ± 1.95
7275.00	111–010	303–202	P	70	0.36	16	1.43 ± 0.82	3.95 ± 0.16
7273.00	101–000	101–000	P	0	9.62	2	1.62 ± 0.66	Base
7259.33	210–010	221–110	O	45	0.46	51	3.99 ± 0.21	2.16 ± 1.16
7252.01	101–000	422–423	O	297	1.23	11	3.62 ± 0.95	5.19 ± 1.93
7250.07	200–000	221–212	O	61	0.65	33	4.36 ± 0.40	Base
	111–010	212–111	P					
7240.42	101–000	221–220	P	136	6.53	1	4.31 ± 0.10	Shape

associated with the total nuclear spin angular momentum. With identical hydrogen atoms (H) in spatially symmetric locations, the H_2O molecule shows the intrinsic property to exist in two distinct species (ortho and para), depending on the orientation of nuclear spins of its H atoms.

Each hydrogen atom in water has a magnetic moment, which is associated with the proton's spin of value $1/2$. When the spins are parallel, there is a paramagnetic state called ortho-H_2O with a total nuclear spin $I = 1$. This is the triplet state $[(\uparrow\uparrow), 1/\sqrt{2}\,(\uparrow\downarrow + \uparrow\downarrow), (\downarrow\downarrow)]$, i.e., with three symmetric spin states characterized by nuclear spin projected values $M_I = (+1, 0, -1)$. When the spins are anti-parallel there is the nonmagnetic state called para-H_2O with total nuclear spin $I = 0$ and the component along a defined axis $M_I = 0$. This state is described by one anti-symmetric spin state $1/\sqrt{2}\,(\uparrow\downarrow - \uparrow\downarrow)$.

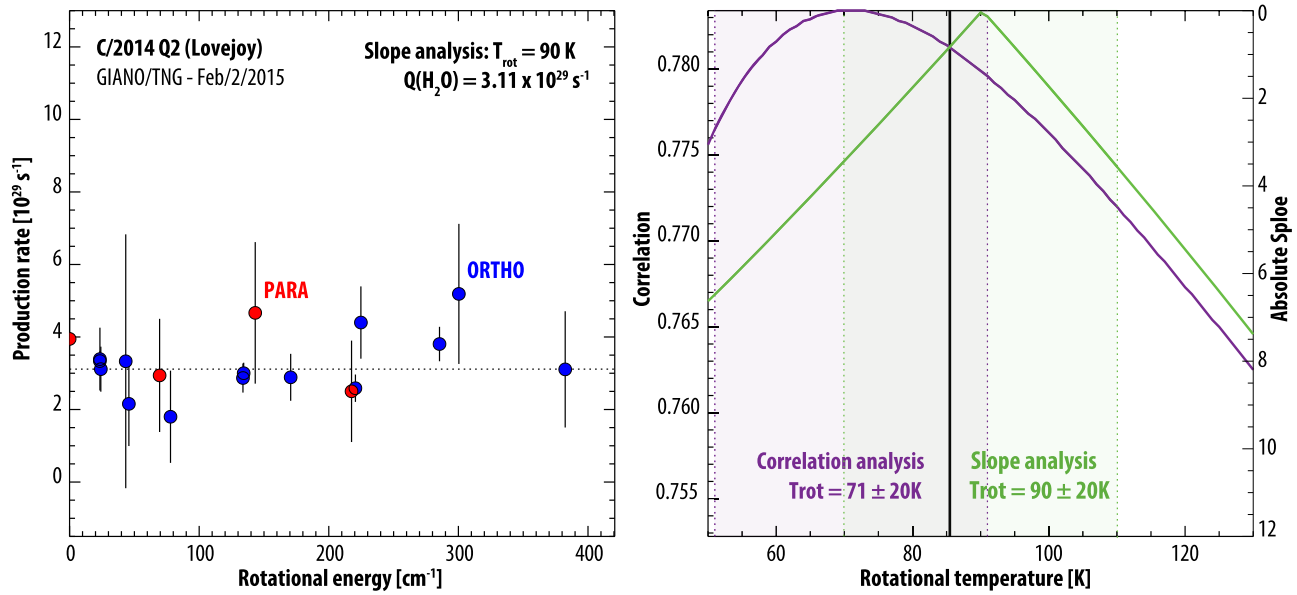

Figure 6. Determination of the rotational temperature of H_2O in comet Lovejoy. Left: the slope analysis method. The x-axis represents the mean lower rotational energy [cm^{-1}] of the principal pumping transitions and the y-axis represents the water production rate [$Q(H_2O)$, units of 10^{29} s^{-1}] extracted from an individual line. A specific value of T_{rot}, and the summed g-factor for each line is recalculated for each value assumed; a linear fit to the data provides a slope. The process is continued at 1 K intervals, over the range 50–150 K. The water production rates [ortho (blue) and para (red)] are evaluated by assuming the abundance ratio of ortho- and para-water was 3, i.e., the measured values of water production rate for the full-water model. The graphic shows the line-by-line values of $Q(H_2O)$ returned for $T_{rot} = 90$ K, and the linear fit (dotted line; slope = zero). Right: comparison of the slope and correlation analyses. The x-axis represents the rotational temperature T_{rot} [K]. The scale for the correlation coefficient appears on the left y-axis and the scale for absolute values of slope appears on the right y-axis. The graphic shows the comparison between T_{rot} derived from the slope method (green) and from the correlation method (purple).

Even though both spin isomers species are water, the ortho and para forms of water are two distinct molecules with distinct energy levels. The difference between the lowest para energy level and the lowest ortho energy level is about 23.8 cm^{-1} (~34 K), meaning that the ratio between the total populations of ortho and para states (the OPR) depends on the temperature (T_{spin}) at which the molecules were formed. For example at temperature $T = 0$ K the equilibrium ratio of water isomers is all para, because the lowest para energy level (000) is 23.8 cm^{-1} below the lowest ortho level. For temperature $T > 50$ K the most stable ratio of ortho- and para-water is 3:1.

The probability of permutation between ortho- to para-water is almost zero; indeed it is possible to have a conversion between them only via molecule breaking and later reformation.[14] Exchange transitions between the two isomer species, whether radiative or collisional, are forbidden by quantum mechanical selection rules. This leads to the idea that the relative abundance of the nuclear spin species remains largely unchanged for billions of years (Mumma & Charnley 2011, and references therein). If so, the spin temperature would reflect the formation temperature of the molecule.

The idea to retrieve an OPR for water in the cometary coma is linked with the measure of the chemical formation temperature of water in the early phase of solar system formation. The OPR in cometary water was measured for the first time in 1P/Halley (Mumma et al. 1987, 1988), and the low values of T_{spin}, found in the pre-perihelion evaluation (~35 K) and post-perihelion evaluation (>40 K), suggested that the conditions of the formative stage of our planetary system were preserved.

There is a strong debate on the reliability of the OPR property as signature information about the original temperature of the molecule's formation. It is almost evident that H_2O molecules preserve the nuclear spin during their long residence in the interior of a comet and probably during the sublimation process, but our knowledge about the nuclear spin conversion is still meager. Although this debate is strong, the evaluation of T_{spin} is an important diagnostic in order to study the origin of cometary material. From our measurements we achieve an OPR = (2.70 ± 0.76), but the confidence limits are not small enough to enable a critical test of the nuclear spin temperature.

4. CONCLUSION

The collected data allowed us to obtain the following results.

1. We detected 52 water lines in the 2 and 1.4 μm regions of the GIANO echellogram. These lines belong to eight vibrational water bands. In the 2 μm region, across orders #39, #40, #41, we detected two bands of non-resonance fluorescence (111–100 and 021–010) and one band (011–000) of resonance fluorescence. In the 1.4 μm region, across orders #53, #54, #53, #56, we detected three non-resonant bands (201–100, 111–010, and 210–010), and two resonant bands (200–000 and 101–000).
2. Through the slope analysis method we obtained a rotational temperature $T_{rot} = 90$ K. This is the temperature in the ground ro-vibrational state that best fitted (with slope zero) the ratio of observed and predicted fluxes (F_{obs}/F_{pred}) with respect to the mean value of rotational state energies in the ground vibrational state.

[14] Another possibility has been studied by Limbach et al. (2006), in which the spin conversion can happen on ice surfaces. This leads to thinking that the measured OPR in cometary coma, for gas released from a cold icy nucleus, could reflect the nucleus surface temperature.

3. At $T_{rot} = 90$ K we achieved a total water production rate, for the nucleus-centered region, of about $Q(H_2O) = (3.11 \pm 0.14) \times 10^{29}$ s^{-1}. The production rates obtained for ortho-water and para-water are $Q(H_2O)^{ORTHO} = (2.33 \pm 0.11) \times 10^{29}$ s^{-1} and $Q(H_2O)^{PARA} = (0.87 \pm 0.21) \times 10^{29}$ s^{-1} respectively, before seeing corrections are applied.
4. In order to correct for "slit losses" due to atmospheric seeing, we evaluated the growth factor for a fiber-fed spectrograph (see Appendix D). Our evaluation ($Q_{scale}^{GIANO} = 1.6$) allowed us to obtain a water production rate of $Q(H_2O) = (4.98 \pm 0.22) \times 10^{29}$ s^{-1}, in agreement with (Paganini et al. 2015).
5. From our measurements of ortho- and para-water production rates we achieve an OPR $= (2.70 \pm 0.76)$. The confidence limits obtained with our retrieval were not small enough to enable an accurate test of the nuclear spin temperature.

APPENDIX A

Table 4 summarizes the wavelength coverage of the 50 orders of the GIANO echellogram. The spectral order number (from 32 to 80) is reported in the first column. For each order, the central wavelength λ_0, the beginning and the ending wavelengths λ_{min} and λ_{max} are shown in columns 2 through 4. Column 5 ($\Delta\lambda$) represents the wavelength subtended by each pixel. The table is provided by GIANO/TNG web page (see http://www.tng.iac.es/instruments/giano/#manuals).

APPENDIX B

Table 5 summarizes the results of the flux calibration process. The first column shows the GIANO spectral order number. Columns 2 and 3 report the mean wavelength (λ) and wavelength subtense per pixel ($\Delta\lambda$) evaluated during the calibration. Column 4 reports the mean flux of the calibration star for each order, while the signal-to-noise ratio (S/N) obtained during flux calibration is shown in column five. Columns 6–9 report the mean flux calibration factors (Γ coefficients) obtained for each track (Topmost, Midup, Middown, and Lowest) and for each order (from 32 to 80).

APPENDIX C

The GIANO spectrograph is equipped with a Hawaii-II PACE detector. The acquisition system of GIANO saves multiple non-destructive read-out frames in the local data archive. The number N of non-destructive reads depends on integration time. The system acquires a frame every 10 s, so for an exposure time of 300 s the number of non-destructive reads will be 30. These read-out frames are analyzed with the "Flower ramp analysis," that is performed after the integration (Oliva et al. 2012). If I is the intensity for unit of time and for pixel, every non-destructive read will produce a signal I^*t. This analysis consists in the linear fit of measured intensity I, of the N sampled reads, with respect to the time t. The error on the fitting allows us to obtain a read-out noise of only 5 e$^-$/pix. The dark current and internal background of the instrument present a value of about 0.05 e$^-$/s. This value is close to the 0.033 e$^-$/s reported on the detector data-sheet provided by the manufacturer.

During the observations of 2015 February 2 we collected 10 dark frames, 11 sky frames and 5 nodding (AB) frames on comet Lovejoy (see Table 2). During the data reduction process the frames were arranged as follows: from the 10 dark frames and the 11 sky frames we estimated a mean dark frame

Table 4
Central, Beginning, and Ending Wavelength for Each Spectral Order

Spectral Order Number	λ_0 (μm)	λ_{min} (μm)	λ_{max} (μm)	$\Delta\lambda$ (10^{-4} μm)
32	2.397	2.369	2.423	0.256
33	2.325	2.297	2.349	0.249
34	2.256	2.230	2.280	0.242
35	2.192	2.166	2.215	0.235
36	2.131	2.106	2.153	0.229
37	2.073	2.049	2.095	0.222
38	2.019	1.995	2.040	0.217
39	1.967	1.944	1.988	0.211
40	1.917	1.895	1.938	0.206
41	18706	1.849	1.890	0.201
42	1.826	1.805	1.845	0.196
43	1.784	1.763	1.802	0.191
44	1.743	1.723	1.761	0.187
45	1.704	1.684	1.722	0.183
46	1.667	1.648	1.685	0.179
47	1.632	1.613	1.649	0.175
48	1.597	1.579	1.614	0.172
49	1.565	1.547	1.581	0.168
50	1.533	1.516	1.550	0.165
51	1.503	1.486	1.519	0.161
52	14744	1.457	1.490	0.158
53	1.447	1.430	1.462	0.155
54	1.420	1.403	1.435	0.152
55	1.394	1.378	1.409	0.150
56	1.369	1.353	1.383	0.147
57	1.345	1.329	1.359	0.144
58	1.322	1.306	1.336	0.142
59	1.299	1.284	1.313	0.140
60	1.277	1.263	1.291	0.137
61	1.256	1.242	1.270	0.135
62	1.236	1.222	1.249	0.133
63	1.217	1.202	1.229	0.131
64	1.197	1.184	1.210	0.129
65	1.179	1.165	1.192	0.127
66	1.161	1.148	1.173	0.125
67	1.144	1.131	1.156	0.123
68	1.127	1.114	1.139	0.121
69	1.111	1.098	1.122	0.119
70	1.095	1.082	1.106	0.118
71	1.079	1.067	1.091	0.116
72	1.064	1.052	1.075	0.114
73	1.050	1.037	1.061	0.113
74	1.035	1.023	1.046	0.111
75	1.021	1.010	1.032	0.110
76	1.008	0.996	1.019	0.108
77	0.995	0.983	1.005	0.107
78	0.982	0.971	0.992	0.106
79	0.970	0.958	0.980	0.104
80	0.957	0.946	0.968	0.103

Note. The nominal pixel subtense is also given for each order.

Table 5
The Γ Coefficients for All 4 Tracks of the Two Fibers (A and B)

Spectral Order Number	λ (nm)	Δλ (nm)	Flux 10^{-17}(W cm^{-2} μm^{-1})	S/N	Γ coefficients 10^{-17}(W cm^{-2} μm^{-1}/(ADU/s))			
					Track Positions on Array (1, 2), and Fiber id (A, B)[a]			
					Topmost (B3)	Midup (B4)	Middown (A1)	Lowest (A2)
32	2396.0752	0.02616	2.19	30.9	1.13	2.40	1.15	2.48
33	2323.4006	0.02536	2.92	38.3	1.31	2.81	1.35	2.93
34	2254.9998	0.02460	3.64	53.8	1.52	3.28	1.58	3.46
35	2190.5103	0.02389	4.37	66.9	1.63	3.45	1.66	3.69
36	2129.6035	0.02323	5.10	79.8	1.69	3.67	1.77	3.93
37	2071.9900	0.02259	5.82	61.1	1.85	4.08	1.95	4.38
38	2017.4086	0.02199	6.55	53.3	2.03	4.53	2.15	4.82
39	1965.6276	0.02142	7.28	36.3	2.14	4.80	2.27	5.13
40	1916.4349	0.02088	8.00	95.5	2.01	4.56	1.97	4.39
41	1869.6422	0.02037	8.73	241.2	2.12	4.98	2.17	4.77
42	1825.0779	0.01988	9.45	79.4	2.51	5.77	2.60	5.95
43	1782.5868	0.01941	10.2	35.6	3.03	6.88	3.25	7.50
44	1742.0265	0.01897	10.9	67.7	3.41	7.72	3.67	8.46
45	1703.2695	0.01854	11.6	80.1	3.74	8.50	4.04	9.30
46	1666.1976	0.01813	12.4	78.0	4.11	9.34	4.42	10.2
47	1630.7023	0.01774	13.8	93.0	4.63	10.6	5.03	11.4
48	1596.6864	0.01737	15.3	66.4	5.29	12.1	5.75	13.1
49	1564.0587	0.01701	16.9	72.0	6.01	13.8	6.53	14.9
50	1532.7363	0.01667	18.4	88.8	6.77	15.6	7.34	16.7
51	1502.6404	0.01634	19.9	40.7	7.51	17.3	8.10	18.5
52	1473.7025	0.01602	21.5	26.3	8.25	19.1	8.87	20.3
53	1445.8564	0.01571	23.0	25.9	8.93	20.9	9.63	22.0
54	1419.0410	0.01542	24.5	27.8	9.27	22.0	9.94	22.5
55	1393.1998	0.01514	26.1	84.1	9.71	23.0	10.1	22.3
56	1368.2816	0.01486	27.6	89.5	10.0	23.9	10.0	22.3
57	1344.2369	0.01460	29.1	23.2	11.5	27.1	12.3	28.3
58	1321.0204	0.01434	30.7	26.1	12.2	33.0	15.1	34.8
59	1298.5907	0.01410	32.2	75.2	14.3	33.8	15.4	35.6
60	1276.9080	0.01386	33.7	56.9	15.9	37.4	17.1	39.5
61	1255.9349	0.01363	35.3	75.0	16.5	38.9	18.0	40.8
62	1235.6377	0.01341	36.8	97.5	17.3	40.9	18.6	42.6
63	1215.9846	0.01319	38.3	71.6	18.3	43.3	19.6	44.9
64	1196.9447	0.01298	39.9	55.5	19.5	46.3	20.8	47.7
65	1178.4895	0.01278	41.4	45.7	20.7	52.0	22.1	50.6
66	1160.5929	0.01258	43.0	26.6	22.5	53.5	23.9	54.8
67	1143.2297	0.01239	44.5	18.4	24.3	58.4	25.7	58.7
68	1126.3765	0.01221	46.0	16.4	26.3	62.8	27.6	62.9
69	1110.0103	0.01203	47.6	22.3	27.8	66.5	29.1	66.4
70	1094.1111	0.01185	49.1	54.3	30.1	72.2	31.6	72.0
71	1078.6583	0.01168	50.6	82.5	31.7	76.3	33.2	75.9
72	1063.6345	0.01152	52.2	98.4	34.0	82.2	35.5	80.8
73	1049.0200	0.01136	53.7	110.9	36.5	88.1	37.9	85.2
74	1034.8013	0.01120	55.2	106.8	39.0	94.0	40.2	91.4
75	1020.9597	0.01105	56.8	101.8	41.7	100	42.7	97.3
76	1007.4813	0.01090	58.3	86.2	44.9	109	45.9	116
77	994.3517	0.01076	59.9	91.2	54.3	132	56.2	123
78	981.5579	0.01062	61.4	51.6	78.9	299	75.1	167
79	969.0867	0.01048	62.9	21.7	151	361	133	290
80	956.9262	0.01035	64.5	11.6	366	869	301	620

Note.
[a] See Figure 1 for positions of A and B fibers on sky, and Figure 2 for track positions of image slices (two for each fiber) on the array detector.

(hereafter D_m) and a mean sky frame (hereafter S_m). From the 5 nodding frames on the comet we estimated an A-fiber centered mean frame and a B-fiber centered mean frame (hereafter $C^A{}_m$ and $C^B{}_m$). The reduction proceeded as follows: we subtracted the mean dark frame from the mean sky frame (S_m–D_m, hereafter S_D) and we subtracted the mean dark frame from the A-fiber centered comet mean frame and the B-fiber centered comet mean frame ($C^A{}_m$–D_m, hereafter A_D and $C^B{}_m$–D_m, hereafter B_D). Finally we subtracted the dark subtracted mean sky frame from the two dark subtracted mean comet frames

(A_D–S_D, hereafter A and B_D–S_D, hereafter B). The *Giano_tools* extracts the 1D spectrum from these cleaned cometary A-frame and B-frame (see Section 2.2).

The expected noise of a single dark frame can be estimated with the following equation:

$$N_D = \sqrt{(D^*t_{\rm int}) + {\rm RON}^2}$$

while the expected noise of the mean dark frame can be obtained by dividing the noise on the single dark frame by the square-root of the number of dark frames.

$$N_{Dm} = \frac{N_D}{\sqrt{n_{\rm dark}}}$$

where D is the dark current [0.05 e^-/s/pix], RON is the read-out noise [5 e^-/pix] (reported in Table 1), $n_{\rm dark}$ [10 frame] is the number of dark frames, $t_{\rm int}$ [300 s] is the integration time (reported in Table 2).

The expected noise on the mean dark frame is 2.0 e^-(0.9 ADU) per pixel. This value is in agreement with the measured noise on the mean dark frame of about 2.6 e^- (1.2 ADU).

The expected noise on the 1D sky spectrum, extracted from the mean sky echellogram through *Giano_tools*, can be estimated using the following formula:

$$N_{Sm} = \frac{\sqrt{(S^*G) + (D^*t_{\rm int}{}^*n_{\rm pix}^y) + ({\rm RON}^2{}^*n_{\rm pix}^y)}}{\sqrt{n_{\rm sky}}}$$

where S is the measured signal on the sky spectra [about 14 ADU], D is the dark current [0.05 e^-/s/pix], G is the gain of the detector [2.2 e^-/ADU], RON is the read-out noise [5 e^-/pix] (see Table 1), $t_{\rm int}$ [300 s] is the integration time (see Table 2), $n_{\rm pix}^y$ [4 pix] is the number of row-pixels on the single arch-shaped track from which we extracted a 1D spectrum adding together the signal of each pixels (see Section 2.2 and Figure 2) and $n_{\rm sky}$ [11 frame] is the number of sky frames.

Due to the fact that each mean sky frame has been dark (mean frame) subtracted, the noise on the mean sky spectrum is obtained by the square root of the square noise of mean sky spectrum plus the square noise of mean dark multiplied for the same number of row-pixels $n_{\rm pix}^y$ [4 pix] from which we extracted the sky spectrum.

$$N_{Sm}^{\rm tot} = \sqrt{N_{Sm}^2 + (N_D^2{}^*n_{\rm pix}^y)}.$$

The expected noise of the mean sky spectrum is 5.8 e^- (2.6 ADU). This value is in agreement with the measured noise on the sky spectrum of about 6.4 e^- (2.9 ADU).

For the comet we have two different cleaned frames: the frame in which the nucleus is centered on fiber A (the coma in sampled in fiber B) and the frame in which the nucleus is centered in fiber B (the coma in sampled in fiber A). From these frames the *Giano_tools* extracts, for each order of GIANO echellogram, four 1D spectra, that we call track 1, 2, 3 and 4 (see Section 2.2 and Figure 2). In the A-centered frame, the two spectra coming from sliced fiber A (tracks 1 and 2) are sampling the nucleus and the two spectra coming from sliced fiber B (tracks 3 and 4) are sampling the coma; for the B-centered frame the situation is exactly the opposite: tracks 1 and 2 of A fiber are sampling the coma and tracks 3 and 4 of fiber B are sampling the nucleus. We chose to estimate the expected noise for order 40 of the A-centered frame. We did the estimation of noise both for a 1D spectrum sampling the nucleus (track 1) and a 1D spectrum sampling the coma (track 4).

In order 40 we detected seven water lines, so we evaluated the noise both considering the signal of line plus cometary continuum and considering the signal from the cometary continuum.

The expected noise on the mean comet spectrum sampling the nucleus (A-centered frame, track 1 or 2 and B-centered frame, track 3 or 4) or sampling the coma (A-centered frame, track 3 or 4 and B-centered frame, track 1 or 2) has been estimated using the following formula line by line (here we are showing the A-centered frame, track 1, for clarity):

$$N_{C_{\rm A,A1}^{\rm line+cont}} = \frac{\sqrt{(C_{\rm A,A1}^{\rm line+cont}{}^*G) + (D^*t_{\rm int}{}^*n_{\rm pix}^y{}^*n_{\rm pix}^\lambda) + ({\rm RON}^2{}^*n_{\rm pix}^y{}^*n_{\rm pix}^\lambda)}}{\sqrt{n_A}}$$

$$N_{C_{\rm A,A1}^{\rm line+cont}}^{\rm tot} = \sqrt{(N_{C_{\rm A,A1}^{\rm line+cont}})^2 + (N_{Sm})^2{}^*n_{\rm pix}^\lambda}$$

$$N_{C_{\rm A,A1}^{\rm cont}} = \frac{\sqrt{(C_{\rm A,A1}^{\rm cont}{}^*G) + (D^*t_{\rm int}{}^*n_{\rm pix}^y{}^*n_{\rm pix}^\lambda) + ({\rm RON}^2{}^*n_{\rm pix}^y{}^*n_{\rm pix}^\lambda)}}{\sqrt{n_A}}$$

$$N_{C_{\rm A,A1}^{\rm cont}}^{\rm tot} = \sqrt{(N_{C_{\rm A,A1}^{\rm cont}})^2 + (N_{Sm})^2{}^*n_{\rm pix}^\lambda}$$

Considering that the line flux is obtained as: $C_{\rm A,A1}{}^{\rm line} = C_{\rm A,A1}{}^{\rm line+cont} - C_{\rm A,A1}{}^{\rm cont\text{-}model}$, the expected noise on the detected lines is:

$$N_{C_{\rm A,A1}^{line}}^{\rm tot} = (N_{C_{\rm A,A1}^{\rm line+cont}})$$

where $C_{\rm A,A1}{}^{\rm line+cont}$ is the integrated flux under the line plus continuum [ADU], $C_{\rm A,A1}{}^{\rm cont\text{-}model}$ is the model of the continuum (no noise) in [ADU], obtained using the advanced GENLN3 terrestrial model (Edwards 1992; Villanueva et al. 2015) that synthesizes the transmittance and radiance spectra of Earth's atmosphere. The subscript (A,A1) means that we are considering the nucleus centered on fiber A and we are considering the track 1 of fiber A. D is the dark current [0.05 e-/s/pix], G is the gain of the detector [2.2 e-/ADU], RON is the read-out noise [5 e-/pix] (reported in Table 1), $n_{\rm A}$ is the number of A comet frames, $t_{\rm int}$ is the integration time [300 s] (reported in Table 2) and $n_{\rm pix}^\lambda$ is the number of pixel under the line [5 pix] from which we estimated the integrated flux and $n_{\rm pix}^y$ [4 pix] is the number of row-pixels on the single arch-shaped track from which we extracted a 1D spectrum. Table 6 shows the estimated values of noise for order 40, A-centered fiber, on track A1, i.e., an area sampling the nucleus while in Table 7 the estimated values of noise for order 40, A-centered fiber, on track B4, i.e., an area sampling the coma, are reported.

To compare the expected noise with respect the measured noise on comet spectra we inserted in the *Calib_giano* routine the possibility of computing the noise during the calibration. The noise is computed on the residual spectra after model of transmittance subtraction.

In the following table values of measured noise on order 40 both of the A-centered and B-centered fibers are reported:

Table 6
Expected Noise Line by Line on Order 40 A-centered Fiber Track A1 (on Nucleus)

Frequency (cm^{-1})	$(C \pm N^{tot})_{A,A1}^{line+cont}$(ADU)[a]	$(C \pm N^{tot})_{A,A1}^{cont}$(ADU)[a]	$(C \pm N^{tot})_{A,A1}^{line}$(ADU)[a]	S/N
5252.39	99.12 ± 7.74	62.19 ± 7.52	36.93 ± 7.74	3.4
5215.04	170.89 ± 8.15	138.04 ± 7.97	32.85 ± 8.15	2.9
5199.75	239.73 ± 8.53	172.47 ± 8.16	67.26 ± 8.53	5.7
5194.56	230.62 ± 8.48	204.93 ± 8.34	25.69 ± 8.48	2.2
5194.28	231.45 ± 8.48	204.93 ± 8.34	26.52 ± 8.48	2.2
5187.98	80.81 ± 7.63	4.18 ± 7.16	76.63 ± 7.63	7.3
5175.41	159.64 ± 8.09	144.39 ± 7.70	15.25 ± 8.09	1.4

Note.
[a] The integration of flux is done on five pixels covering the detected line.

To compare the measured noise with respect the expected noise it is necessary to take into account of the number of pixels, $n_{\rm pix}^{\lambda}$ [5 pix] on which the signal has been integrated.

For track A1 of the A-centered fiber (sampling the nucleus) the measured noise will be (see Table 8): 7.8 e^-/pix (3.6 [ADU/pix]) which, rescaled to $\sqrt{n_{\rm pix}^{\lambda}}$ gives a value of about 17.4 e^- (7.9 [ADU]). This value is in agreement with expected noise of about 17.2 e^-/pix (7.8 [ADU/pix]) evaluated on the continuum. For track B4 of of the A-centered fiber (sampling the coma) the measured noise will be: 6.7 e^-/pix (3.1 [ADU/pix]) which, taking into account of $\sqrt{n_{\rm pix}^{\lambda}}$ gives a value of about 15.2 e^- (6.9 [ADU]). This value is in agreement with the expected noise of about 16.5 e^-/pix (7.5 [ADU]) evaluated on the continuum.

As explained in Section 2.2 and shown in Figure 4, the *Calib_giano* routine produces three distinct residual 1D spectra combining the tracks sampling the nucleus (the *center* spectrum) and the tracks sampling the upper and lower parts of the coma (the *coma up* and the *coma down* spectra):

$$I_{\rm nucl} = \frac{I_{\rm A1}^{\rm A\text{-}centered} + I_{\rm A2}^{\rm A\text{-}centered} + I_{\rm B3}^{\rm B\text{-}centered} + I_{B4}^{\rm B\text{-}centered}}{2}$$

$$I_{\rm coma\_up} = I_{\rm B3}^{\rm A\text{-}centered} + I_{B4}^{\rm A\text{-}centered}$$

$$I_{\rm coma\_down} = I_{\rm A1}^{\rm B\text{-}centered} + I_{\rm A2}^{\rm B\text{-}centered}$$

From the usual propagation of the errors, the expected noise on these three spectra has been evaluated as follows, with the assumption that the noises are more or less the same:

$$N_{\rm nucl} = \frac{\sqrt{(N_{\rm A1}^{\rm A\text{-}centered})^2 (N_{\rm A2}^{\rm A\text{-}centered})^2 + (N_{\rm B3}^{\rm B\text{-}centered})^2 + (N_{B4}^{\rm B\text{-}centered})^2}}{2} \approx N_{\rm A1}^{\rm A\text{-}centered}$$

$$N_{\rm coma\_up} = \sqrt{(N_{\rm B3}^{\rm A\text{-}centered})^2 + (N_{B4}^{\rm A\text{-}centered})^2} \approx \sqrt{2}{}^{*} N_{B4}^{\rm A\text{-}centered}$$

$$N_{\rm coma\_down} = \sqrt{\frac{(N_{\rm A1}^{\rm B\text{-}centered})^2 + (N_{\rm A2}^{\rm B\text{-}centered})^2}{2}} \approx \sqrt{2}{}^{*} N_{\rm A1}^{\rm B\text{-}centered}$$

The expected noise on the nucleus spectrum is 17.2 e^- (7.8 [ADU]), while the measured noise, rescaled by $\sqrt{n_{\rm pix}^{\lambda}}$, the pixels on which the signal has been integrated, is about 29.0 e^-/pix (13.2 [ADU]) (see Table 8). The expected noise on the coma spectra is 23.5 e^- (10.7 [ADU]) while the measured noise, rescaled by $\sqrt{n_{\rm pix}^{\lambda}}$, is about 23.6 e^-/pix (10.7 [ADU/pix]). We note that the noise is dominated by read-out noise and dark current noise. The measured noise on the nucleus combined spectra seems higher with respect to the expected noise on the coma combined spectra, probably because of the larger contribution of cometary continuum in some parts of the spectrum between the absorption features of the atmosphere.

APPENDIX D

Fiber's growth factor: variability between nucleus and coma spectra. To derive the global production rate a detailed study of nucleus outgassing is necessary, i.e., how does the gas dynamically propagate in the coma? Species that are released directly from the nucleus are called *primary molecules*. They can produce *product species* by photo-dissociation and/or photo-ionization processes. Gas generated by these two mechanisms shows different radial distributions in the coma and an analysis of spatial distribution is essential to discriminate between them. For a spherically symmetric release, a primary molecule shows a column density that varies according to the Haser model as $(e^{-\rho/L})/\rho$, where ρ is the nucleocentric distance projected along the line of sight and L is the molecular scale length. In the approximation $\rho \ll L$, the column density has a behavior of $1/\rho$. For a product species the variation of column density with respect to ρ is much flatter. Examples of anisotropies and asymmetries in the gas distributions due to non-isotropic outgassing have been observed with radio or long-slit IR and UV spectroscopy. Indeed, the picture presented here is simplistic, but space dictates omission of additional details.

With long-slit spectroscopy it is possible to estimate the global production rate, through a detailed analysis of the spatial profiles for observed molecules in the coma, compensating for "slit losses" (caused by atmospheric seeing) by employing the so called "Q-curve" methodology (Dello Russo et al. 1998; Villanueva et al. 2011a).

The "seeing" is the effect produced by the turbulence of Earth's atmosphere that introduces blurring and twinkling on astronomical objects. This effect produces a spread of flux from a point source causing the loss of flux in the central part of the object. The flux from a star (or comet) is then less sharply peaked and thus somewhat less intense in the nucleus region than it would be if seeing were absent. A circular aperture that is smaller than the point-spread function (PSF) will thus

Table 7
Expected Noise Line by Line on Order 40 A-centered Fiber Track B4 (on coma)

Frequency (cm^{-1})	$(C \pm N^{tot})_{A,B4}{}^{line+cont}$(ADU)[a]	$(C \pm N^{tot})_{A,B4}{}^{cont}$(ADU)[a]	$(C \pm N^{tot})_{A,B4}{}^{line}$(ADU)[a]	S/N
5252.39	42.90 ± 7.40	24.09 ± 7.29	18.81 ± 7.40	1.8
5215.04	76.56 ± 7.61	63.06 ± 7.53	13.51 ± 7.61	1.3
5199.75	104.66 ± 7.77	89.53 ± 7.69	15.12 ± 7.77	1.4
5194.56	157.70 ± 8.08	90.20 ± 7.69	67.50 ± 8.08	6.1
5194.28	123.75 ± 7.89	90.20 ± 7.69	33.55 ± 7.89	3.0
5187.98	40.40 ± 7.39	8.35 ± 7.18	32.05 ± 7.39	3.1
5175.41	76.58 ± 7.61	70.00 ± 7.67	6.58 ± 7.61	0.6

Note.
[a] The integration of flux is done on five pixels covering the detected line.

Table 8
Measured Noise on Order 40

	Fiber and Track	Noise (ADU/pix)
Fiber A centered on nucleus		
sampling on nucleus	$(A1)^n$	3.56
sampling on nucleus	$(A2)^n$	4.84
sampling on coma up	$(B3)^u$	2.99
sampling on coma up	$(B4)^u$	3.07
Fiber B centered on nucleus		
sampling on coma down	$(A1)^d$	2.73
sampling on coma down	$(A2)^d$	3.21
sampling on nuclues	$(B3)^n$	3.53
sampling on nuclues	$(B4)^n$	5.15
Combined spectra		
Nucleus	$[(A1)^n + (A2)^n + (B3)^n + (B4)^n]/2$	5.9
Coma up	$(B3)^u + (B4)^u$	4.8
Coma down	$(A1)^d + (A2)^d$	4.8

measure a reduced flux from the object. This effect is called "slit or aperture loss."

The usual "*Q*-curve" analysis, developed for long-slit spectroscopy, corrects for "slit losses" by multiplying the measured Q (obtained with Equation (3.5)) by a *growth factor* (Q_{scale}) derived by spatial profile analysis. The method is based on the evaluation of apparent production rates at regular intervals along the slit, assuming uniform symmetric outflow (Q_{-n},..., Q_{-2}, Q_{-1}, Q_0, Q_1, Q_2, …Q_n). Each value is called a "spherical production rate" because a spherically symmetric outflow is assumed when relating the local flux measurement to an apparent production rate (the up- and down-slit profiles are first averaged to remove asymmetries.[15]

The "*nucleus-centered production rate*" (Q_{NC}) is the production rate measured in the region close to the nucleus, $Q_{NC} = \langle Q_0, \langle Q_1 \rangle \rangle$. The *terminal production rate* is defined as the value of Q evaluated far from the nucleus, along the slit, $Q_{Term} = \langle \langle Q_2 \rangle, \langle Q_3 \rangle, ..., \langle Q_n \rangle \rangle$. The increase of the mean values of Q from the nucleus-centered position to the terminal position defines the "growth factor" that is quantified by the ratio of the terminal production rate and the nucleus-centered production rate as shown in the following formula:

$$Q_{scale} = \frac{Q_{Term}}{Q_{NC}} = \frac{\langle Q_2, Q_3, ..., Q_n \rangle}{\langle Q_0, Q_1 \rangle} \quad (3.6)$$

The usual retrieval method for long-slit spectroscopy to evaluate the final production rate is not applicable for fiber-fed spectroscopy. Indeed it is not possible to perform the standard analysis of *spherical production rate* in the region close to the nucleus and then the evaluation of terminal production rate, recovering the growth factor (Q_{scale}) in order to estimate the total production rate corrected for seeing.

In our observation method, the nodding on comet with two fibers allows us to sample three different regions of the comet (the *coma up*, the *nucleus*, and the *coma down*), as shown in Figures 1 and 3. After symmetrizing, we have only two points representing the values of column densities in the nucleus-centered region, and in the coma centered 3″ away from the nucleus, instead of a complete spatial profile. However, experience with long-slit spectrographs shows that the terminal value is invariably reached by 3″ from the nucleus. We obtain the following estimation of column densities: $\sigma^{CENTER} = (6.29 \pm 0.27) \times 10^{20}$ [mol m^{-2}] and $\sigma^{2100} = (1.36 \pm 0.10) \times 10^{20}$ [mol m^{-2}] at 55 K (σ^{2100} is the mean of σ^{DOWN} and σ^{UP}, where $\sigma^{DOWN} = (0.94 \pm 0.13) \times 10^{20}$ [mol m^{-2}] and $\sigma^{UP} = (1.78 \pm 0.16) \times 10^{20}$ [mol m^{-2}] at $T_{rot} = 50$ K and 60 K respectively, obtained with slope analysis). Application of a Haser model to these column densities using appropriate parameters then permits determination of a growth factor for the fiber-fed case. The expected Haser $f(x)$ for a 1″ aperture at the center is $f^{CENTER} = 0.00533$, and $f^{2100} = 0.00073$ at 3″ from the nucleus. Consequently, $Q_{scale} = (\sigma^{2100}/f^{2100})/(\sigma^{CENTER}/f^{CENTER}) = 1.6$.

We also considered a method for obtaining Q_{scale} from the mean nucleus-centered column density (and Q_{NC}) if we assume a value for the PSF introduced by "seeing." Then, the amount of the flux lost by the "seeing" effect is obtained from the following formula:

$$Q_{Scale}^{FIBER} = \frac{\sum_{FIberFov} ModeledFluxTOA}{\sum_{FiberFov} ObservedFlux}. \quad (3.7)$$

This represents the ratio between the value of the cometary modeled flux at top of the atmosphere integrated in the fiber field

[15] The mean value of $\langle Q_j \rangle$ taken at symmetric positions with respect the center position Q_0 (i.e., Q_{-i} and Q_i) allows us to correct for non-symmetric outflow.

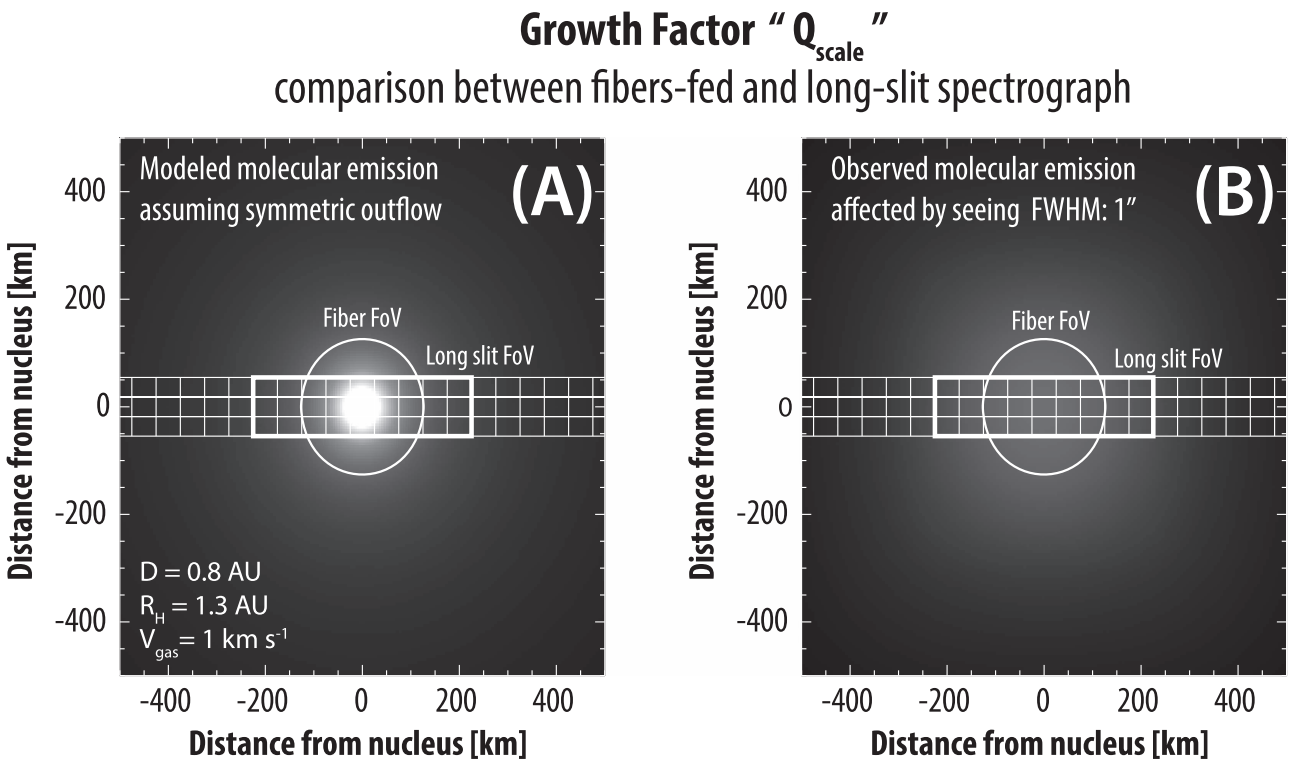

Figure 7. Determination of growth factor ($Q_{\rm scale}$) and comparison of long-slit and fiber-fed spectroscopy methods. In both panels, the *x*- and *y*-axes represent the distance from the photometric nucleus (km). Left: cometary 2D model of expected outgassing with isotropic outflow, for a comet like C/2014 Q2 Lovejoy. The integration areas for long slit and fiber-fed are represented by the square and the circle. Right: the effect of seeing on modeled outgassing data. The ratio between the modeled flux sampled by the fiber field of view in panel (A) with respect to the observed flux (seeing affected) sampled by the fiber field of view in panel (B) defines the fiber growth factor. The same ratio integrated in the long-slit field of view gives the comparison value for long-slit spectroscopy.

of view (Figure 7, panel A), and the observed flux ("seeing" affected), integrated over the fiber field of view (Figure 7, panel B).

We report the comparison between the growth factor ($Q_{\rm scale}$) for the GIANO fiber-fed spectrograph and a long-slit spectrograph[16] in Figure 6. Considering a typical seeing of 0.″8 for the site, we estimate a value of $Q_{\rm scale}$ for the GIANO fibers of ${Q_{\rm scale}}^{\rm Fiber} = 1.6$; consistent with the observed loss observed between the center and up/down fibers.

REFERENCES

Altwegg, K., Balsiger, H., Bar-Nun, A., et al. 2015, Sci, 347, 1261952
Bockelée-Morvan, D., Biver, N., Swinyard, B., et al. 2012, A&A, 544, L15
Combes, M., Crovisier, J., Encrenaz, J., et al. 1988, Icar, 76, 404
Combes, M., Moroz, V. I., Crifo, J. F., et al. 1986, SvAL, 12, 257
Crovisier, J., Brooke, T. Y., Hanner, M. S., et al. 1996, A&A, 315, L385
Crovisier, J., & Encrenaz, Th. 1983, A&A, 126, 170
Dello Russo, N., DiSanti, M. A., Mumma, M. J., Magee-Sauer, K., & Rettig, T. W. 1998, Icar, 135, 377
Dello Russo, N., Mumma, M. J., DiSanti, M. A., et al. 2000, Icar, 143, 324
Dello Russo, N., Mumma, M. J., DiSanti, M. A., & Magee-Sauer, K. 2002, JGRE, 107, 5095
Edwards, D. P. 1992, GENLN2: A General Line-by-Line Atmospheric Transmittance and Radiance Model version 3.0, NCAR Technical Note NCAR/TN-367+STR (Boulder, CO: The National Center for Atmospheric Research)
Hartogh, P., Lis, D. C., Bockelée-Morvan, D., et al. 2011, Natur, 478, 218
Gomes, R., Levison, H. F., Tsiganis, K., & Morbidelli, A. 2005, Natur, 435, 466
Greenstein, J. L. 1958, ApJ, 128, 106
Izidoro, A., de Souza Torres, K., Winter, O. C., & Haghighipour, N. 2013, ApJ, 767, 54
Jewitt, D., Morbidelli, A., & Rauer, H. 2008, in Saas-Fee Advance Course 35, Trans-Neptunian Objects and Comets, 132
Larson, H. P., Davis, D. S., Mumma, M. J., et al. 1986, ApJL, 309, L95
Limbach, H. H., Buntkowsky, J., Matthes, S., et al. 2006, Chem. Phys. Chem., 7, 551
Lis, D. C., Bockelée-Morvan, D., Boissier, J., et al. 2008, ApJ, 675, 931
Morbidelli, A., Morbidelli, A., Chambers, J., et al. 2000, M&PS, 35, 1309
Mumma, M. J., Blass, W. E., Weaver, H. A., & Larson, H. P. 1988, BAAS, 20, 826
Mumma, M. J., & Charnley, S. B. 2011, ARA&A, 49, 471
Mumma, M. J., DiSanti, M. A., Dello Russo, N., et al. 1996, Sci, 272, 1310
Mumma, M. J., DiSanti, M. A., & Xie, X. 1995, IAU Circ., 6228, 2
Mumma, M. J., Kostiuk, T., Buhl, D., Chin, G., & Zipoy, D. 1982, OptEn, 21, 313
Mumma, M. J., Weaver, H. A., & Larson, H. P. 1987, A&A, 187, 419
Mumma, M. J., Weaver, H. A., Larson, H. P., Williams, M., & Davis, D. S. 1986, Sci, 232, 1523
Oliva, E., Biliotti, V., Baffa, C., et al. 2012, Proc. SPIE, 8453, 84532T
Oliva, E., Origlia, L., Maiolino, R., et al. 2013, A&A, 555, A78
Oliva, E., Origlia, L., Scuderi, S., et al. 2015, A&A, 581, A47
Paganini, L., Mumma, M. J., Gibb, E. L., et al. 2015, AAS Meeting, 47, 415.11
Swings, P. 1941, PLicO, Bulletin, 19, 131
Villanueva, G. L., Mumma, M. J., Bonev, B. P., et al. 2012, JQSRT, 113, 202
Villanueva, G. L., Mumma, M. J., DiSanti, M. A., et al. 2011a, Icar, 216, 227
Villanueva, G. L., Mumma, M. J., & Magee-Sauer, K. 2011b, JGRE, 116, 1
Villanueva, G. L., Mumma, M. J., Novak, R. E., et al. 2015, Sci, 348, 218
Weaver, H. A., & Mumma, M. J. 1984, ApJ, 276, 782
Weaver, H. A., Mumma, M. J., Larson, H. P., & Davis, D. S. 1986, Natur, 324, 441
Xie, D. X., & Mumma, M. J. 1996, ApJ, 464, 457
Xie, X., & Mumma, M. J. 1992, ApJ, 386, 720
Yamamoto, T. 1982, A&A, 109, 326

[16] The comparison has been done for NIRSPEC, the long-slit IR spectrograph at the W. M. Keck Observatory, Mauna Kea, Hawaií.